Article

Cell Metabolism

Functional Gut Microbiota Remodeling Contributes to the Caloric Restriction-Induced Metabolic Improvements

Graphical Abstract

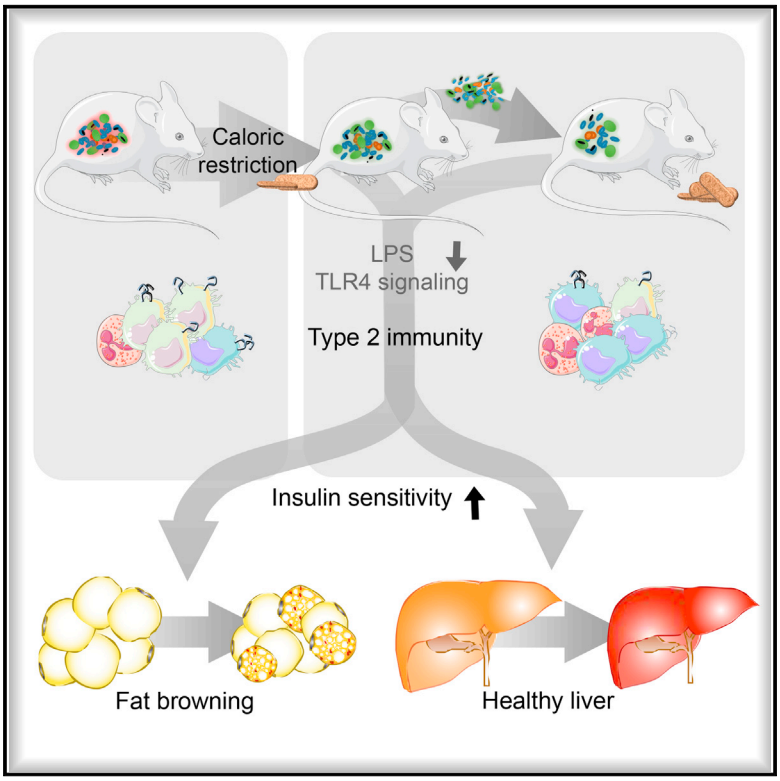

Authors

Salvatore Fabbiano, Nicolas Suárez-Zamorano, Claire Chevalier, ..., Andrew Macpherson, Jacques Schrenzel, Mirko Trajkovski

Correspondence

mirko.trajkovski@unige.ch

In Brief

Fabbiano et al. show that gut microbiota remodeling is important for the metabolic improvements associated with caloric restriction, including fat browning and improved glycemic control. They link the systemic beneficial metabolic effects to reduced endotoxin production, leading to increased type 2 immune response in the adipose tissue.

Highlights

- CR-microbiota transplantation improves glycemic control and insulin sensitivity
- CR microbiota promotes beige fat development and reduces weight gain
- CR suppresses key microbial genes for LPS biosynthesis and dictates the immune tone
- LPS-TLR4 inhibition in bone marrow-derived cells improves metabolism and browning

Fabbiano et al., 2018, Cell Metabolism *28*, 907–921
December 4, 2018
https://doi.org/10.1016/j.cmet.2018.08.005

CellPress

Cell Metabolism
Article

Functional Gut Microbiota Remodeling Contributes to the Caloric Restriction-Induced Metabolic Improvements

Salvatore Fabbiano,[1,2] Nicolas Suárez-Zamorano,[1,2] Claire Chevalier,[1,2] Vladimir Lazarević,[3] Silas Kieser,[1,2] Dorothée Rigo,[1,2] Stefano Leo,[3] Christelle Veyrat-Durebex,[1,2] Nadia Gaïa,[3] Marcello Maresca,[4] Doron Merkler,[5] Mercedes Gomez de Agüero,[6] Andrew Macpherson,[6] Jacques Schrenzel,[3] and Mirko Trajkovski[1,2,7,8,*]

[1]Department of Cell Physiology and Metabolism, Centre Médical Universitaire, Faculty of Medicine, University of Geneva, 1211 Geneva, Switzerland
[2]Diabetes Centre, Faculty of Medicine, University of Geneva, 1211 Geneva, Switzerland
[3]Genomic Research Lab, Division of Infectious Diseases, Geneva University Hospitals, 1211 Geneva, Switzerland
[4]Discovery Biology, Discovery Sciences, IMED Biotech Unit, AstraZeneca Gothenburg, Mölndal 43183, Sweden
[5]Department of Pathology and Immunology, Centre Médical Universitaire, Faculty of Medicine, University of Geneva, 1211 Geneva, Switzerland
[6]Maurice Müller Laboratories (DKF), Universitätsklinik für Viszerale Chirurgie und Medizin Inselspital, University of Bern, 3010 Bern, Switzerland
[7]Institute of Genetics and Genomics in Geneva, University of Geneva, 1211 Geneva, Switzerland
[8]Lead Contact
*Correspondence: mirko.trajkovski@unige.ch
https://doi.org/10.1016/j.cmet.2018.08.005

SUMMARY

Caloric restriction (CR) stimulates development of functional beige fat and extends healthy lifespan. Here we show that compositional and functional changes in the gut microbiota contribute to a number of CR-induced metabolic improvements and promote fat browning. Mechanistically, these effects are linked to a lower expression of the key bacterial enzymes necessary for the lipid A biosynthesis, a critical lipopolysaccharide (LPS) building component. The decreased LPS dictates the tone of the innate immune response during CR, leading to increased eosinophil infiltration and anti-inflammatory macrophage polarization in fat of the CR animals. Genetic and pharmacological suppression of the LPS-TLR4 pathway or transplantation with *Tlr4*$^{-/-}$ bone-marrow-derived hematopoietic cells increases beige fat development and ameliorates diet-induced fatty liver, while *Tlr4*$^{-/-}$ or microbiota-depleted mice are resistant to further CR-stimulated metabolic alterations. These data reveal signals critical for our understanding of the microbiota-fat signaling axis during CR and provide potential new anti-obesity therapeutics.

INTRODUCTION

Caloric restriction (CR) up to 40% of nutritious diet intake reduces body weight and total fat amount, delays the onset of multiple age-associated diseases, and improves metabolic health (Canto and Auwerx, 2011; De Guzman et al., 2013; Ocampo et al., 2012). CR is a potent physiological stimulus that promotes functional beige fat development (Fabbiano et al., 2016), which contributes to the inguinal subcutaneous adipose tissue (ingSAT) loss during CR. The CR-induced browning is concomitant with increased type 2 immune signaling, which is necessary for the beige fat development and a number of metabolic improvements caused by CR (Fabbiano et al., 2016). The intestinal microbiota can influence the whole-body metabolism by affecting energy balance (Turnbaugh et al., 2009, 2006; Koren et al., 2012; Liou et al., 2013; Ridaura et al., 2013; Sekirov et al., 2010; Backhed et al., 2004; Suarez-Zamorano et al., 2015; Thaiss et al., 2016), and has profound effects on fat morphology, function, and amount (Suarez-Zamorano et al., 2015; Chevalier et al., 2015; Li et al., 2017). These observations indicate the existence of a microbiota-fat signaling axis; however, the mechanisms, and the microbial signals and functional alterations causing the phenotypic and morphological changes that regulate energy homeostasis of the new host following microbiota transplantation, remain poorly understood. It is also not clear whether the gut microbiota affects the metabolic alterations during CR. Here we demonstrate that microbiota remodeling is an important contributor of beige fat induction during CR, and a key factor that promotes the metabolic improvements caused by CR, including improved insulin sensitivity, glucose tolerance, and lowered fat gain. Moreover, we provide a mechanistic explanation of the microbiota-derived signals that regulate the tone of the innate immune response during CR, necessary for the CR-induced metabolic alterations. These data reveal signals critical for our understanding of the microbiota-fat signaling axis, and suggest new anti-diabetes and anti-obesity therapeutics.

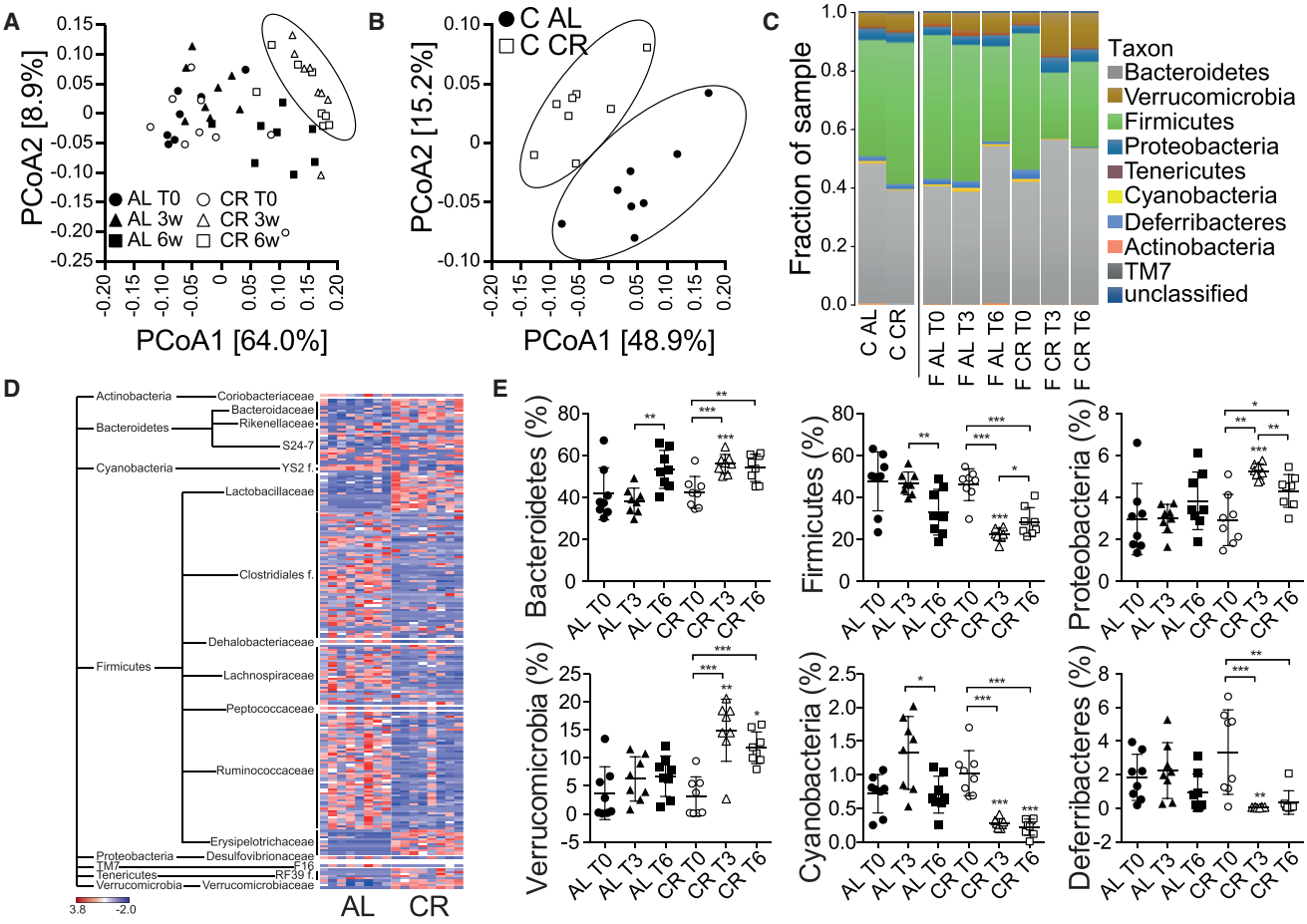

Figure 1. Short-Term Caloric Restriction Changes the Gut Microbiota Composition

(A and B) Principal coordinate analysis of fecal (A) (Adonis test p = 0.519 at time 0, p = 0.001 at 3 weeks, and 0.013 at 6 weeks) and cecum (B) (Adonis test, p = 0.002) samples performed by computing weighted UniFrac. Each symbol represents a fecal (A) or cecum (B) sample from caloric-restricted (CR) or their *ad libitum*-fed (AL) control mice at the beginning of the experiment (T0), after 3 and 6 weeks (T3 and T6, respectively) (n = 8 per group).

(C) Comparison of phylum-level proportional abundance of cecum and feces of AL and CR mice at the indicated time points.

(D) Heatmap showing OTUs associated with a p value of <0.05 between AL and CR in feces. Plotted is a *Z* score (scale shown in color bar) computed on the relative abundances of the selected OTUs across AL and CR samples. An idealized tree represents the taxonomic hierarchy of their phyla and families. Final leaves are labeled with the corresponding family name.

(E) Relative abundance of different phyla in feces. Each graph represents the sum of the sequences annotated with the phylum relative to all analyzed sequences. Significance in (E) was calculated using non-paired two-tailed Student's t test.*p $\leq$ 0.05, **p $\leq$ 0.01, ***p $\leq$ 0.001.

RESULTS

Short-Term Caloric Restriction Changes the Gut Microbiota Composition

Thirty days of 40% CR, but without malnutrition and lean mass loss, promotes fat browning, suppresses body weight (BW) and white fat mass gain, and improves insulin sensitivity (Figures S1A–S1C) (Fabbiano et al., 2016). This is in part due to the suppressed hepatic glucose production (Barzilai et al., 1998; Barzilai and Gabriely, 2001; Kelley et al., 1993) and the increased glucose uptake in the fat (Fabbiano et al., 2016). To investigate whether short-term CR causes changes in the intestinal microbiota, we collected feces at weeks 0, 3, and 6 and postmortem cecum of CR mice and *ad libitum*-fed (AL) controls. Profiling of the microbiota composition by 16S rRNA gene sequencing, followed by principal coordinates analysis (PCoA), showed alterations of the microbiota content both in cecum and feces samples of CR animals (Figures 1A and 1B). This is in line with the observations that lean human subjects under chronic food restriction with adequate nutrition cluster apart from subjects without dietary restrictions (Griffin et al., 2017). Comparison of phylum-level proportional abundance showed shifts in both cecum and feces (Figure 1C), and the results were confirmed by additional 16S sequencing of an independent set of mice (Figures S1D–S1H). A heatmap of the significantly changed operational taxonomic units (OTUs) in the fecal samples revealed a number of changes within the same families, most notably an increase in Lactobacillaceae and Erysipelotichaceae during CR and decrease in other Firmicutes families, as well as increased Bacteroidaceae and Verrucomicrobiaceae, the latter represented by *Akkermansia muciniphila* (Figures 1D and 1E). Members of these families were among the most significantly

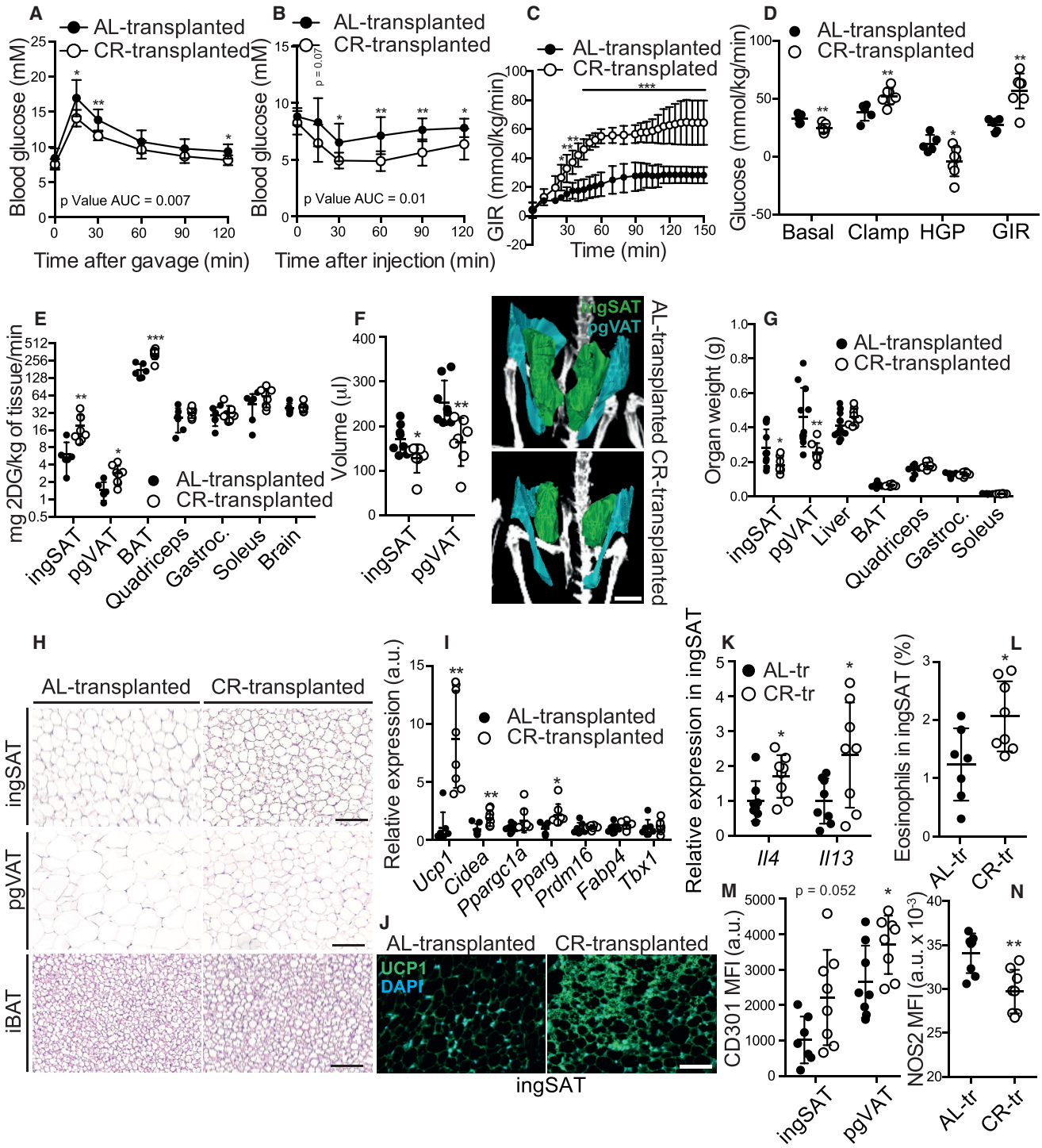

Figure 2. Gut Microbiota Remodeling during Caloric Restriction Provides Metabolic Benefits

(A and B) Oral glucose tolerance test (OGTT) (A) and insulin tolerance test (ITT) (B) of AL- and CR-microbiota-transplanted GF mice (n = 6 per group). AUC, area under the curve.

(C–E) Glucose infusion rate (C), 2-DG glucose uptake (D), and glucose disposal (E) in AL- and CR-microbiota-transplanted GF mice (n = 6 per group).

(F) Quantification of the total ingSAT and pgVAT volume and their 3D reconstitution using the MicroPET-CT scans from mice as in (A). Scale bar, 2.5 mm.

(G) Weight of indicated organs post mortem of AL- and GF-transplanted mice (n = 6 per group).

(H) Representative H&E-stained histological sections from ingSAT, pgVAT, and iBAT. Scale bar, 200 µm.

(I) Relative mRNA expression of browning markers in ingSAT of AL- and GF-transplanted mice (n = 8 per group).

(J) Representative images of immunofluorescent staining for UCP1 in ingSAT of AL- and GF-transplanted mice. Scale bar, 200 µm.

(legend continued on next page)

changed OTUs using a Kruskal-Wallis test (Figures S1I and S1J). Increase in lactobacilli is linked with beneficial metabolic effects through multiple mechanisms (Fabbiano et al., 2017; Spiljar et al., 2017), while *A. muciniphila* negatively correlates with insulin resistance and adiposity (Dao et al., 2015; Chevalier et al., 2015; Louis et al., 2016; Schneeberger et al., 2015). Opposed to the observations in CR mice, high-fat diet increases the abundance of Tenericutes (Everard et al., 2014) while decreasing bifidobacteria and verrucomicrobia (Schneeberger et al., 2015). Together, these results show a progressive shift in lower gut microbiota composition during energy scarcity, part of which may be correlated with the loss in adiposity and the increased insulin sensitivity.

CR-Microbiota Transplantation Promotes Metabolic Improvements and Fat Browning

To investigate the relevance of the microbiota changes during CR, we transplanted the microbiota from 6-week CR or age-matched AL control mice to germ-free (GF) mice and confirmed the shifts in the recipient mice (Figure S2A). CR-microbiota-transplanted mice showed lower weight gain compared with the AL-transplanted controls without changes in food intake and caloric uptake (Figures S2B–S2D). The CR-microbiota transplantation was sufficient to improve the glucose tolerance after oral glucose gavage and to increase the sensitivity to insulin (Figures 2A and 2B). To further investigate the insulin sensitivity, we performed hyperinsulinemic-euglycemic clamp in awake and unrestrained microbiota-transplanted mice. CR-microbiota transplantation markedly increased the glucose infusion rates needed to maintain the clamped glucose levels, and the stimulated rate of whole-body glucose disappearance levels (Figures 2C and 2D). To investigate peripheral glucose uptake, we co-administered 2-[^{14}C]deoxyglucose (2[^{14}C]DG) during the clamp. While we found no changes in quadriceps, gastrocnemius, or soleus muscle and the brain, the 2[^{14}C]DG administration showed an increased glucose uptake in all adipose tissues of the CR-microbiota-transplanted mice, and a suppressed hepatic glucose production (Figures 2D and 2E). These results were in line with the positron emission tomography-computed tomography (microPET-CT) in non-insulin-stimulated conditions, where the CR-transplanted mice showed increased [^{18}F]fluorodeoxyglucose ([^{18}F]FDG) uptake in the inguinal subcutaneous adipose tissue (ingSAT) (Figures S2E–S2G). CR-transplanted mice showed no changes in their lean mass, but had decreased fat volume and mass (Figures 2F and 2G), in line with the increased number of small multilocular, and a decreased number of large unilocular adipocytes in the ingSAT depots (Figures 2H and S2I). All these characteristics are typical of mature beige adipocytes. Indeed, the CR-transplanted mice had an increased number of UCP1$^+$ cells coupled with markedly enhanced expression of brown fat-specific markers in ingSAT and, to a lesser extent, in the perigonadal visceral adipose tissue (pgVAT) (Figures 2I, 2J, and S2J).

Type 2 immunity potentiates beige fat development in part by alternative activation of M2 polarized macrophages (Nguyen et al., 2011; Chung et al., 2017), possibly through decreased macrophage-mediated norepinephrine degradation (Fischer et al., 2017; Pirzgalska et al., 2017; Camell et al., 2017), and/or suppressed loop of direct M1-mediated inhibition (Chung et al., 2017). Genetic suppression of type 2 immune signaling blocks the browning after cold exposure (Qiu et al., 2014) or CR (Fabbiano et al., 2016). In the ingSAT of the CR-microbiota-transplanted mice we observed increased levels of the type 2 cytokines interleukin-4 (IL-4) and IL-13 (Figure 2K), suggesting that same molecular pathways orchestrate the browning during CR and CR-microbiota transplantation. Accordingly, quantification of the immune cell populations by flow cytometry demonstrated enhanced infiltration of eosinophils and CD301$^+$ M2 polarized macrophages in ingSAT and pgVAT (Figures 2L, 2M, and S2K–S2M), and a marked decrease in NOS2$^+$ M1 macrophages (Figure 2N).

We extended our studies to mice kept at thermoneutrality (Feldmann et al., 2009), and found that CR shifted the microbiota composition also at 30°C (Figure S3A). When transplanting this warm CR-altered microbiota to recipient GF mice that were subsequently also kept at thermoneutrality, we found decreased BW gain without affecting the food intake, increased glucose tolerance and insulin sensitivity, decreased liver, ingSAT, and pgVAT weights, and smaller adipocytes, along with increased fat browning (Figures 3A–3D and S3B–S3E). Compared with the AL CR controls, subjecting GF mice to CR led to decreased weight gain, but this time due to the decrease in both muscle and fat, and an improved glucose tolerance. Remarkably, we could not detect further improvement in insulin sensitivity during CR in absence of microbiota, nor further increase in the browning levels and cold tolerance, despite an the increase in the general adipogenesis markers (Figures 3E–3H and S3F–S3H). Similar effects were seen in antibiotics (Abx)-treated CR mice, where the BW and tissue weight changes were even less pronounced between the CR and AL groups (Figures 3I–3L and S3I–S3K). These results together point out the key contribution of the gut microbiota in mediating a number of CR-induced metabolic benefits, including browning.

CR Leads to Functional Gut Microbiota Alterations

To assess the functional diversity of cecal and fecal microbiota, we performed metagenomics sequencing and functional analysis using the SEED database. Analysis of overall community functional composition with PERMANOVA revealed differences between AL and CR mice in both fecal ($p = 0.0095$) and cecal ($p = 0.027$) samples (Figure 4A). Out of the 35 level-1 subsystems identified, 11 were significantly altered in cecum and 7 in feces. Deeper analysis in cecum and feces samples revealed, respectively, 34 and 23 of the 165 level-2 subsystems,

(K) Relative mRNA expression of type 2 cytokines *Il4* and *Il13* in ingSAT of mice as in (A).
(L) Quantification of eosinophils in stromal vascular fractions (SVF) from mice as in (A).
(M) Quantification of CD301 fluorescence intensity in CD11b$^+$ F4/80$^+$ macrophages from ingSAT SVF of AL- and CR-transplanted GF mice.
(N) NOS2 mean fluorescence intensity (MFI) in macrophages from ingSAT SVF as in (A).
Unless otherwise indicated, error bars show mean ± SD. Significance was calculated using non-paired two-tailed Student's t test. *$p \leq 0.05$, **$p \leq 0.01$, ***$p \leq 0.001$.

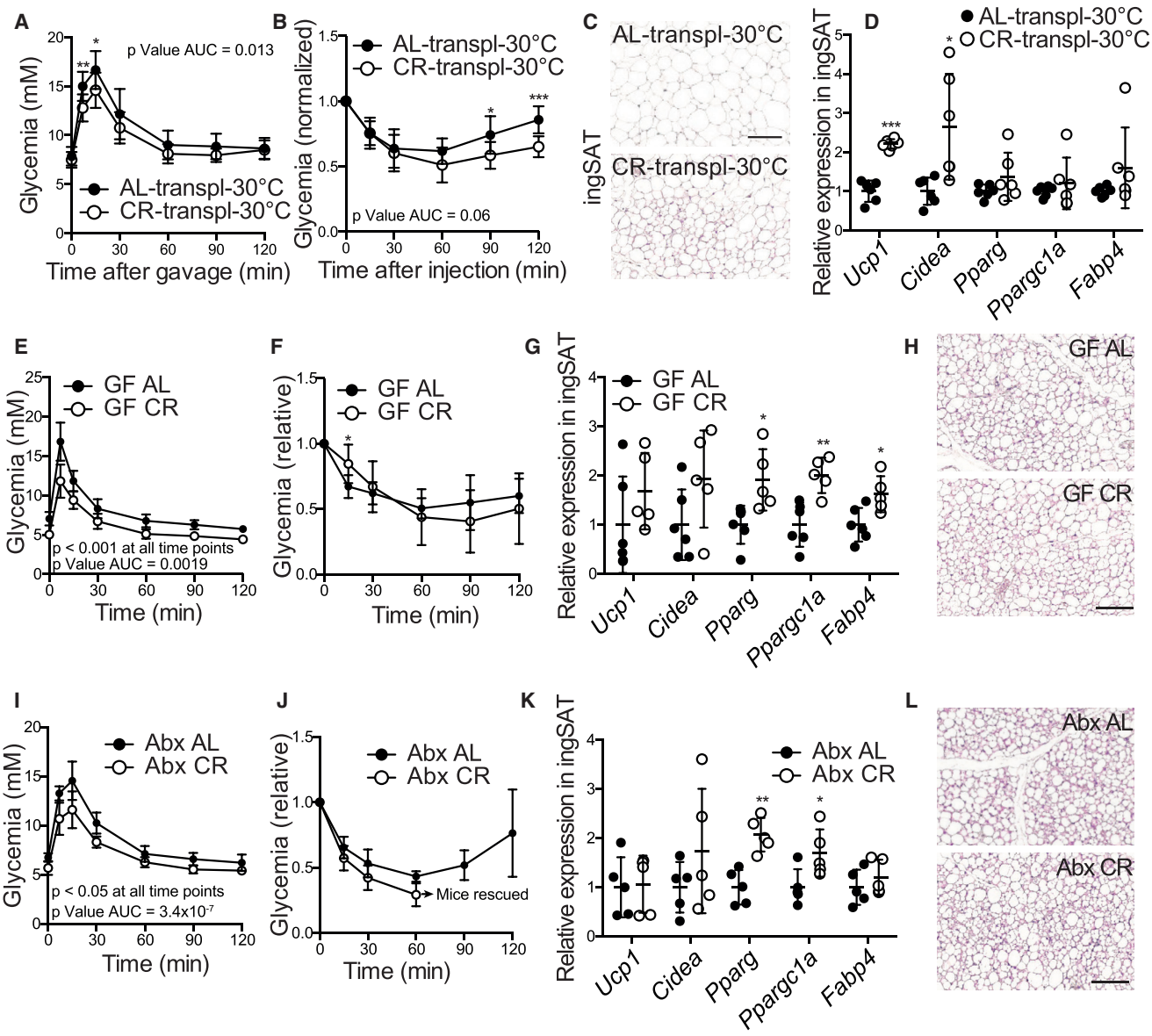

Figure 3. CR Gut Microbiota Transplantation Is Functional at Thermoneutrality

(A and B) OGTT (A) and normalized ITT (B) of thermoneutrality housed AL- and CR-transplanted GF mice (n = 6 per group).

(C) Representative H&E-stained histological sections from ingSAT of mice as in (A). Scale bar, 200 μm.

(D) Relative mRNA expression of browning markers in ingSAT (q) and pgVAT (r) of mice as in (A) (n = 8 per group).

(E and F) OGTT (E) and ITT (F) of mice as in AL and CR GF mice (n = 9–10 per group).

(G) Relative mRNA expression of browning markers in ingSAT of mice as in (E) (n = 5–6 per group).

(H) Representative H&E-stained histological sections from ingSAT of mice as in (E). Scale bar, 200 μm.

(I and J) OGTT (I) and ITT (J) of mice as in AL and CR Abx-treated mice (n = 9–10 per group).

(K) Relative mRNA expression of browning markers in ingSAT of mice as in (E) (n = 5–6 per group).

(L) Representative H&E-stained histological sections from ingSAT of mice as in (E). Scale bar, 200 μm.

Error bars show mean ± SD. Significance was calculated using non-paired two-tailed Student's t test. *p ≤ 0.05, **p ≤ 0.01, ***p ≤ 0.001.

205 and 155 level-3 subsystems, and 1,502 and 1,620 out of 10,862 level-4 functions. To further narrow down relevant functional changes, we focused on level-1 subsystems that showed changes in the same direction in both feces and cecum samples, and found two that satisfied this criterion. The first was the "Arabinose Sensor and Transport" module, which was consistently increased in CR microbiota, likely in response to increased reliance on arabinose in part of the bacterial population during nutrient scarcity (Desai and Rao, 2010). The second was "Cell Wall and Capsule," decreased in CR samples (Figure 4B). This was particularly interesting, since this subsystem includes biosynthesis of lipopolysaccharide (LPS), known to be positively correlated with host BW and insulin resistance (Cani et al., 2007).

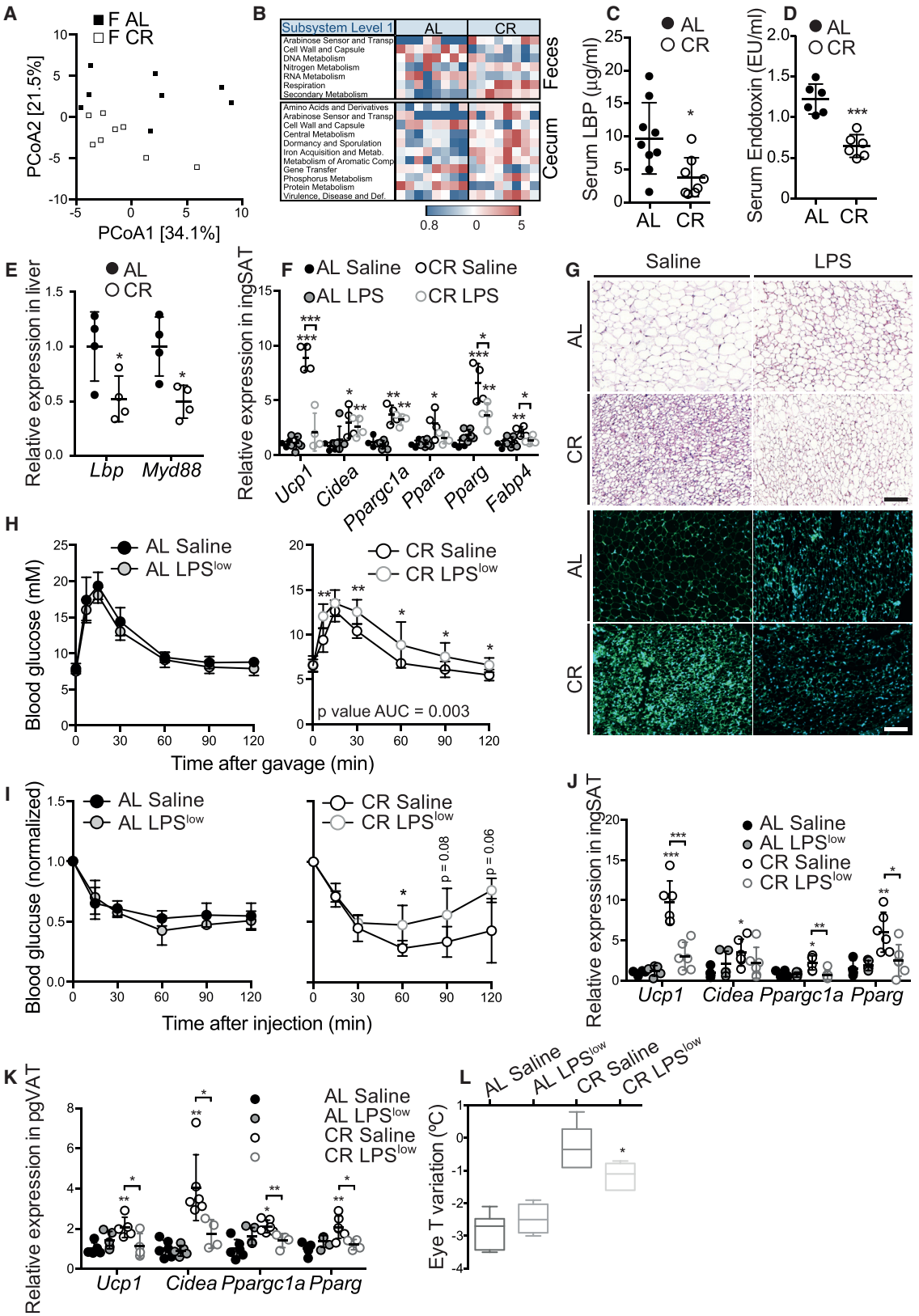

(legend on next page)

LPS Reconstitution Reverts the Metabolic Improvements Caused by CR

Life-long CR enriches phylotypes positively correlated with lifespan (Zhang et al., 2013), concomitant with reduced serum levels of the LPS-binding protein (LBP), manly produced by the liver. High-fat diet and LPS increase are associated with reduced core body temperature and lower heat release, coupled to ER stress and mitochondrial dysfunction (Okla et al., 2015). Moreover, IRF3, which signals downstream of the Toll-like receptor 4 (TLR4), promotes inflammation and decreases browning (Kumari et al., 2016). We found that after 30 days of CR, LBP levels were decreased to similar magnitude as in life-long CR mice (Figure 4C) and the circulating LPS levels in the CR mice were markedly lower compared with AL controls (Figure 4D), along with decreased *Lbp* and *Myd88* liver mRNA expression (Figure 4E). Reconstituting LPS (*Escherichia coli* 055:B5) using osmotic minipumps at dose of 300 μg/kg/day was sufficient to completely revert the CR-mediated increase in the glucose tolerance without affecting the insulin levels during the test, and diminish the improved sensitivity to insulin and cold tolerance (Figures S4A–S4G). LPS replenishment in the CR mice completely prevented the CR-induced browning and the CR-induced increase in the M2 macrophage polarization and eosinophil infiltration (Figures S4H–S4J). Since the LPS-reconstituted CR mice showed 30% higher LPS levels compared with the AL animals, we included additional control AL and CR mice implanted with minipumps releasing ~33% less LPS at 200 μg/kg/day (AL LPS^{low} and CR LPS^{low}, respectively). While the LPS supplementation did not affect the glucose tolerance and insulin sensitivity in the AL mice, its reconstitution markedly suppressed these CR-induced metabolic improvements, the fat browning, and the cold tolerance (Figures 4F–4L), and moderately affected body, fat, and liver weight (Figures S4K–S4N). These results suggest that reconstituting LPS prevents a number of metabolic improvements, as well as the anti-inflammatory type 2 immune response caused by the lower caloric intake.

Hematopoietic TLR4 Suppression Promotes Beige Fat Development

In light of the above data, we assumed that the decreased LPS binding to TLR4 mediates CR-induced browning by modulating the immune tone. To investigate this intriguing hypothesis, we exposed mice to high-caloric diet (HCD) and treated them with the TLR4 inhibitor CLI-095. The treated mice had lower weight gain compared with the HCD-fed control mice despite the constant food intake, and showed improved glucose tolerance and insulin sensitivity (Figures 5A–5C and S5A), consistent with observations in rats (Zhang et al., 2015). In contrast, CLI-095 treatment of *Tlr4* knockout (KO) mice neither changed their BW gain nor the sensitivity to insulin and glucose tolerance (Figures S5B–S5D). The CLI-095-treated mice were resistant to cold stress (Figures 5D and S5E) and their fat mass was lowered, while the lean mass remained constant (Figure 5E). MicroPET-CT showed increased [^{18}F]FDG uptake in ingSAT and a tendency toward increased uptake in the pgVAT in the CLI-095-treated mice (Figures 5F, 5G, S5F, and S5G). Despite the increased glucose uptake in the fat tissues, the fat volume in CLI-095-treated mice was reduced compared with the control animals (Figures 5H and S5H). This was associated with appearance of smaller multilocular adipocytes in the ingSAT, and to a lower extent also in the pgVAT of the CLI-095-treated mice. Accordingly, pharmacological TLR4 inhibition led to marked increase in expression of the browning markers in the ingSAT, evident modestly also in the pgVAT (Figures 5I, 5J, and S5I). This was accompanied with increased type 2 cytokine expression in ingSAT of the treated mice (Figure S5J). These data suggest that pharmacological suppression of TLR4 signaling promotes adipose tissue browning and decreased fat accumulation, associated with improved glucose tolerance and insulin sensitivity.

To directly test the importance of TLR4 downstream signaling in regulating the CR-induced browning, we used the *Tlr4* KO mice. In line with the pharmacological inhibition, genetic TLR4 suppression decreased the weight gain and fat to lean mass ratio compared with the wild-type (WT) controls, and improved the glucose tolerance and the insulin sensitivity at various time points (Figures 5K–5M and S5K–S5N). TLR4 deficiency led to a massive increase in the ingSAT and pgVAT browning (Figures 5N–5P). This conclusion was further corroborated by oxygen consumption rate (OCR) measurements after isoproterenol stimulation using the Seahorse analyzer. The ingSAT fat depots from *Tlr4* KO mice showed increased OCR at basal conditions, and a greater response to β-adrenergic stimuli compared with the corresponding fats from the WT mice (Figure 5Q), suggesting increased thermogenic capacity. Strikingly, while the *Tlr4* KO

Figure 4. LPS Reconstitution Reverts the Metabolic Improvements Caused by CR

(A) PCoA analysis based on Bray-Curtis similarity matrix constructed using the square root-transformed relative abundance of SEED functional roles in AL and CR mice in feces ($p = 0.0095$) samples ($p = 0.027$).

(B) SEED level 1 subsystems significantly different (Wilcoxon rank-sum test, $p < 0.05$) between CR and AL metagenomes (from cecal or fecal samples) are indicated. The level of increase and decrease of the CR/AL ratio of the median relative abundance is indicated by red and blue shading, respectively, according to the color scale.

(C and D) Serum levels of LBP (C) and LPS determined by EndoSafe cartridges (D) in AL and CR mice.

(E) Relative mRNA expression of *Lbp* and *Myd88* in liver of AL and CR mice (n = 4 per group).

(F) Relative mRNA expression of browning markers in ingSAT of sham-operated and LPS-infused AL and CR mice (n = 4–6 per group).

(G) Representative H&E histological sections and immunofluorescent staining for UCP1 from ingSAT of sham-operated and LPS-infused AL and CR mice. Scale bars, 100 μm.

(H and I) OGTT (H) and ITT (I) of sham-operated and LPS-infused AL and CR mice (n = 6 per group).

(J and K) Relative mRNA expression of browning markers in ingSAT (J) and pgVAT (K) of sham-operated AL and CR mice, and LPS-infused AL LPS^{low} and CR LPS^{low} mice (n = 5 per group).

(L) Infrared temperature changes relative to initial values in eye, ventral, or dorsal regions, or eye during 3 hr of cold exposure of mice as in (J) and (K) (n = 5 per group).

Unless otherwise indicated, error bars show mean ± SD and significance was calculated using non-paired two-tailed Student's t test. *$p \leq 0.05$, **$p \leq 0.01$, ***$p \leq 0.001$.

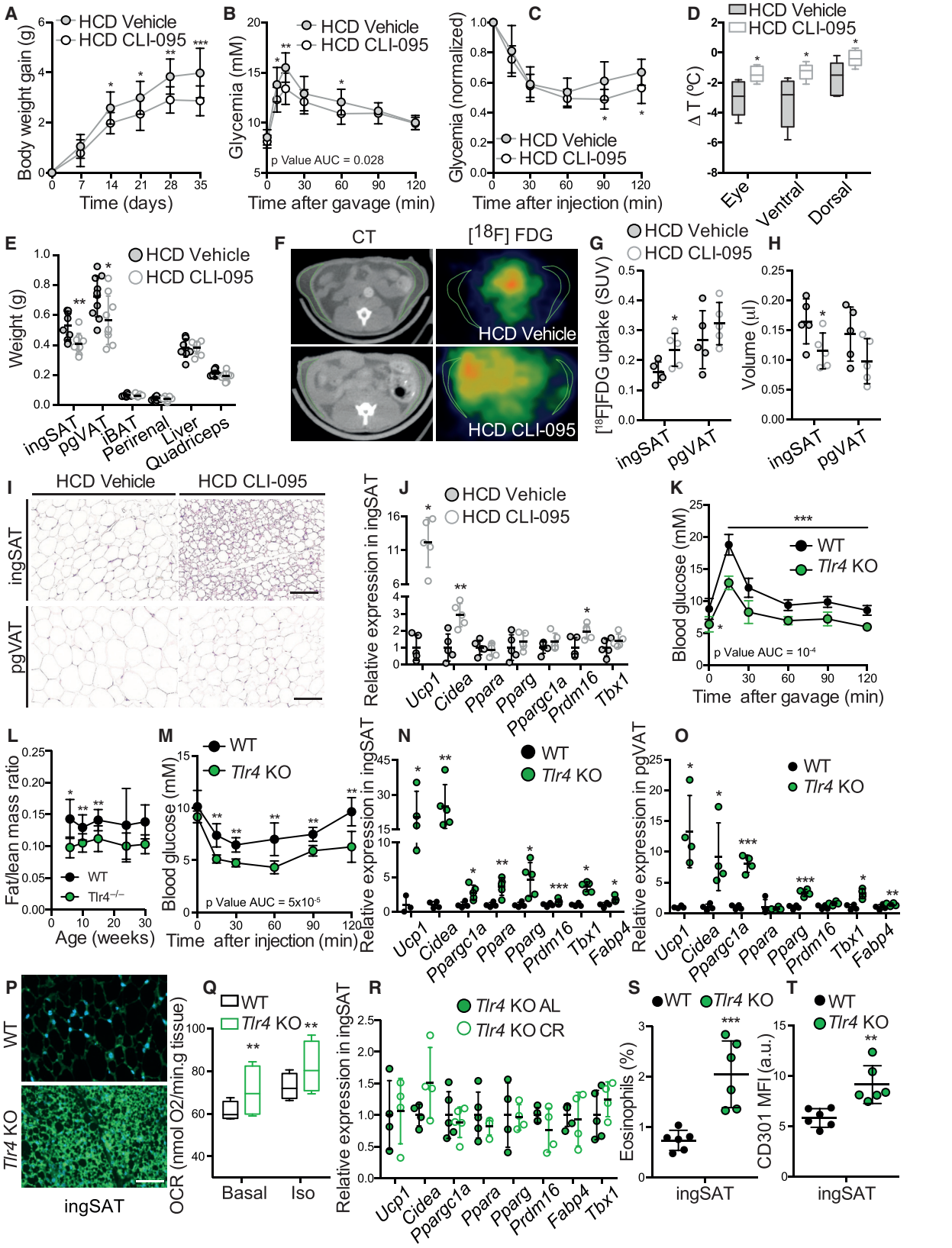

(legend on next page)

and WT mice showed similar LPS levels, CR of the *Tlr4* KO mice neither further promoted weight loss nor improved their thermogenic capacity and browning (Figures 5R and S5O). CR *Tlr4* KO mice showed only mild improvement in the glucose tolerance compared with AL *Tlr4* KO, and no changes in insulin sensitivity despite the similar microbiota changes that were induced in response to CR (Figures S6A–S6H). *Tlr4* KO mice had increased eosinophil infiltration and M2 macrophage polarization in the ingSAT compared with the controls, mimicking the changes induced by CR (Figures 5S and 5T). These results suggest that absence of TLR4 signaling is sufficient to induce browning and improved glycemic control and that it prevents further metabolic improvements caused by CR, including the enhanced beige fat development.

Since suppression of the LPS-TLR4 signaling in CR mice is necessary for the beige fat development and leads to enhanced eosinophil infiltration and M2 macrophage polarization, we sought to directly investigate whether suppression of the TLR4 signaling in the bone marrow-derived hematopoietic cells would mediate the fat browning. We therefore transplanted bone marrow-derived (BMT) cells from the *Tlr4* KO donor mice to lethally irradiated WT or *Tlr4* KO recipients (WT BMT^{KO} or KO BMT^{KO}, respectively), and used WT donor transplantations to irradiated WT or *Tlr4* KO recipients as controls (WT BMT^{WT} or KO BMT^{WT}, respectively) (Figure S6I) and subjected the mice to HCD. The *Tlr4* KO BM recipients displayed improved glucose tolerance and insulin sensitivity (Figures 6A and S6J), consistent with recent observations (Razolli et al., 2015). To investigate the importance of these cells in the beige fat development, we cold-exposed the BMT animals and found that all mice receiving BM cells from *Tlr4* KO mice had improved cold tolerance (Figure 6B) irrespective of the genetic background of the recipients. This was accompanied by smaller adipocytes with multilocular appearance in both ingSAT and pgVAT depots of the mice transplanted with the *Tlr4* KO-derived BM cells and with decreased total fat gain due to lower weight of ingSAT, and to milder extent pgVAT (Figures 6C, 6D, S6K, and S6L). Accordingly, all mice receiving BM from the *Tlr4* KO mice displayed increased browning levels in both white fat depots. Conversely, *Tlr4* KO mice transplanted with WT cells lost most of their browning and their adipose tissues were comparable with the WT mice (Figures 6E and 6F). There were no changes in the LPS levels between the groups (Figure S6M). Together, these data demonstrate that suppression of the TLR4 signaling in the BM-derived cells is sufficient to promote beige fat development irrespective of the genetic background of the recipients, and suggest that the CR-induced browning is mediated by the decreased LPS-TLR4 signaling restricted to these immune cells.

CR-Induced Suppression of the Key Lipid A Biosynthetic Enzymes Underlies the Decreased LPS

CR may affect blood LPS levels by regulating its biosynthesis or by changing the intestinal penetrability. To address the latter, we measured the thickness of the colon mucin layer, a key contributor to the gut barrier function. Analysis of colon Alcian blue staining showed no differences between the groups (Figures 7A and 7B). In addition, 4-kDa fluorescein isothiocyanate (FITC)-dextran gavage revealed no changes in the mucosa-to-blood penetrability, and *intectin* expression was similar between the groups (Figures S7A and S7B). In contrast, analysis of the metagenomics data revealed that Kdo2-lipid A biosynthesis, necessary for the LPS production, was consistently decreased, accompanied by suppressed lipid A-Ara4N pathway (Figures S7D–S7G). Specifically, CR suppressed several critical enzymes including LpxL, LpxB, LpxL, LpxA, and KdtA (or WaaA), all regulating lipid A production (Figures 7C–7G), and LpxK, a key membrane-bound kinase that phosphorylates lipid A disaccharide to produce lipid IV_A as a rate-limiting step (Wang and Quinn, 2010; Emiola et al., 2014). Accordingly, both plasma and feces LPS levels were markedly lower in CR mice (Figures 7H and 7I), suggesting that the suppressed LPS production in the lean mice, and not the changed intestinal permeability seen after very-low-calorie diet in obese female subjects (Ott et al., 2017), underlies the CR-induced reduced LPS levels. This was reflected by reduced expression of *Lbp* and *Myd88* in livers of the GF mice transplanted with CR microbiota (Figure S7H). To investigate

Figure 5. TLR4 Suppression Leads to Beige Fat Development

(A) Body weight gain of HCD mice injected daily with either 10% DMSO (HCD Vehicle) or CLI-095 (HCD CLI-095) for 5 weeks (n = 10).

(B and C) OGTT (B) and normalized ITT (C) of mice as in (A) (n = 10).

(D) Infrared temperature changes relative to initial values in eye, ventral, or dorsal regions, or eye during 3 hr of cold exposure of HCD mice injected daily with either 10% DMSO (HCD Vehicle) or CLI-095 (HCD CLI-095) for 5 weeks (n = 5 per group).

(E) Weight of indicated organs post mortem of mice as in (A) (n = 10 per group).

(F–H) Transversal [^{18}F]FDG PET-CT images (F), standardized uptake values (SUV) of radiolabeled tracer [^{18}F]FDG in ingSAT (G), and quantification of the total ingSAT and pgVAT volume (H) using MicroPET-CT on mice as in (A) (n = 5).

(I) Representative H&E-stained histological sections from ingSAT of HCD vehicle and CLI-095 mice. Scale bar, 200 μm.

(J) Relative mRNA expression of browning markers in ingSAT of HCD Vehicle and CLI-095 mice (n = 5 per group).

(K) OGTT in 8-week-old wild-type (WT) and *Tlr4* KO mice (n = 5–6 per group).

(L) Fat/lean mass ratio in WT and *Tlr4* KO mice at the indicated ages (n = 3–12 per group).

(M) ITT in 8-week-old WT and *Tlr4* KO mice (n = 5–6 per group).

(N and O) Relative mRNA expression of browning markers in ingSAT (N) and pgVAT (O) of WT and $Tlr4^{-/-}$ mice (n = 6 per group).

(P) Representative images of immunofluorescent staining of UCP1 in ingSAT of WT and *Tlr4* KO mice. Scale bar, 200 μm.

(Q) Oxygen consumption rate (OCR) in ingSAT biopsies from WT and *Tlr4* KO mice detected with Seahorse analyzer. Iso, isoproterenol (n = 4 mice per group assayed in quadruplicates).

(R) Relative mRNA expression of browning markers in ingSAT of AL and CR *Tlr4* KO mice (n = 5 per group).

(S and T) Quantification of $CD11b^+Siglec\ F^+$ eosinophils (S) and CD301 mean fluorescence intensity (MFI; T) in $CD11b^+\ F4/80^+$ macrophages in ingSAT SVF of WT and *Tlr4* KO mice (n = 5 per group).

Unless otherwise indicated, error bars show mean ± SD. Significance was calculated using non-paired two-tailed Student's t test.*$p \leq 0.05$, **$p \leq 0.01$, ***$p \leq 0.001$.

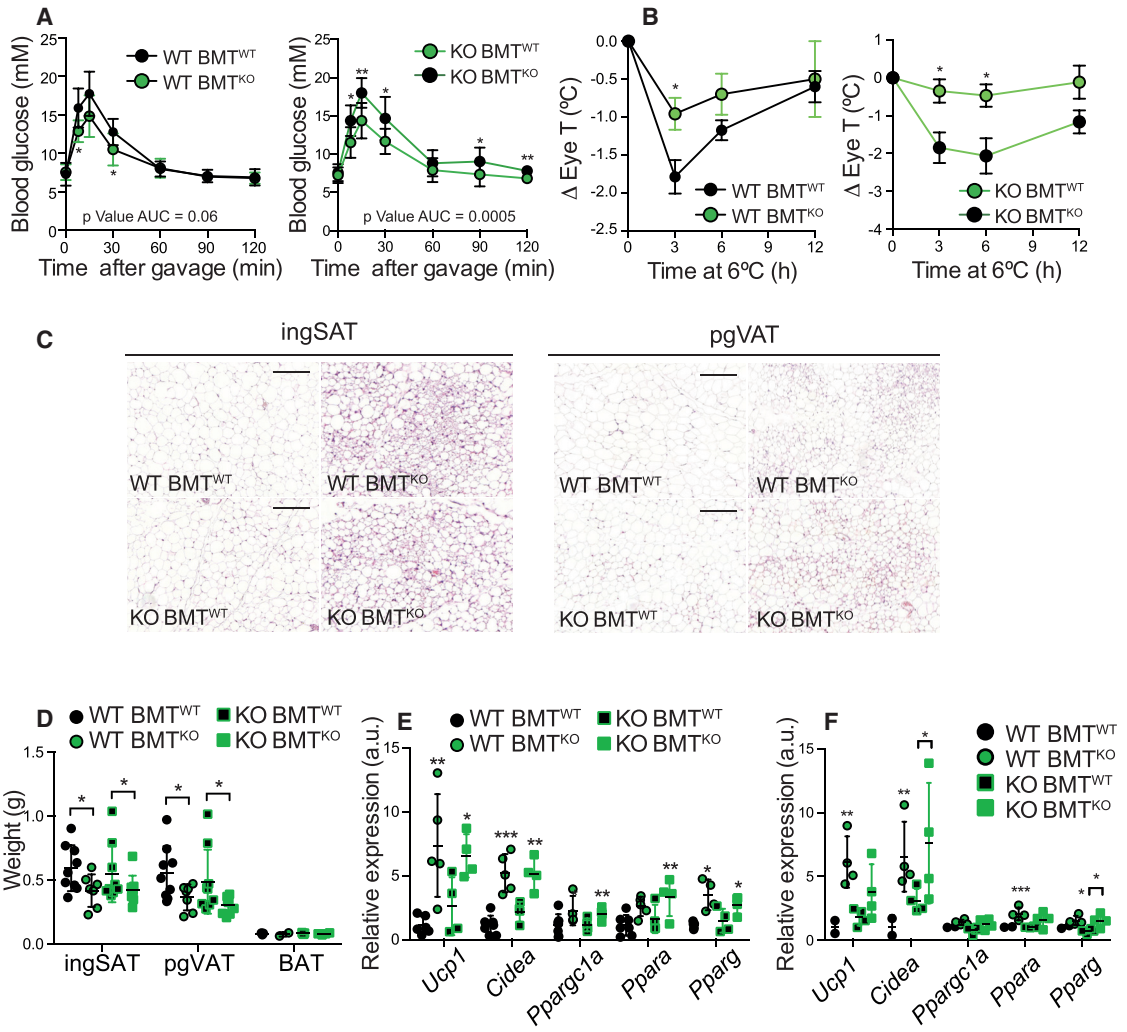

Figure 6. Hematopoietic *Tlr4* Deficiency Promotes Browning

(A) OGTT of WT (left) and *Tlr4* KO (right) mice lethally irradiated and subsequently transplanted with WT and KO bone marrow (n = 5–9 per group).

(B) Infrared eye temperature readings relative to initial values during 12-hr cold-exposed WT (left) and KO (right) BMT mice (*n* = 5–9 per group). Error bars show mean ± SEM.

(C) Representative H&E-stained histological sections from ingSAT and pgVAT of BMT mice (n = 5–9 per group). Scale bars, 200 μm.

(D) Weight of fat depots post mortem in BMT mice (n = 5–9 per group).

(E and F) Relative mRNA expression of browning markers in ingSAT (E) and pgVAT (F) in BMT mice (n = 5–9 per group).

Unless otherwise indicated, error bars show mean ± SD. Significance was calculated using non-paired two-tailed Student's t test. *p ≤ 0.05, **p ≤ 0.01, ***p ≤ 0.001.

the potential importance of the decreased LPS phosphorylation in the browning induction, we used the brush-border enzyme intestinal alkaline phosphatase (iAP), which detoxifies and dephosphorylates LPS (Bentala et al., 2002; Chen et al., 2010) and ameliorates several high-fat-diet-induced metabolic disarrangements (Kaliannan et al., 2013). Oral supplementation of iAP decreased LPS levels in both feces and plasma of HCD-fed mice (Figures 7J and 7K). This led to lower weight gain (starting from the same initial BW), improved glucose tolerance, insulin sensitivity, and cold tolerance of iAP HCD-fed mice without affecting the food and water intake (Figures 7L, 7M, and S7I–S7L). Insulin sensitivity was further investigated using hyperinsulinemic-euglycemic clamp in awake and unrestrained HCD-fed mice. iAP administration led to a marked increase in the glucose infusion rates needed to maintain euglycemia (Figure 7N). While no changes were observed in 2[^{14}C]DG uptake in quadriceps muscle and brain (Figure S7K), iAP supplementation increased glucose uptake in ingSAT and markedly suppressed the hepatic glucose production (Figure 7O). These results suggest that suppressed hepatic glucose production and increased glucose uptake in ingSAT are main drivers of the improved glucose phenotype after iAP treatment. Since HCD leads to fatty liver, and TLR4 deficiency in hepatocytes improves hepatic steatosis after high-fat feeding (Jia et al., 2014), we investigated the liver morphology in HCD-fed mice treated with CLI-095 or iAP. Both pharmacological treatments potently ameliorated fatty liver

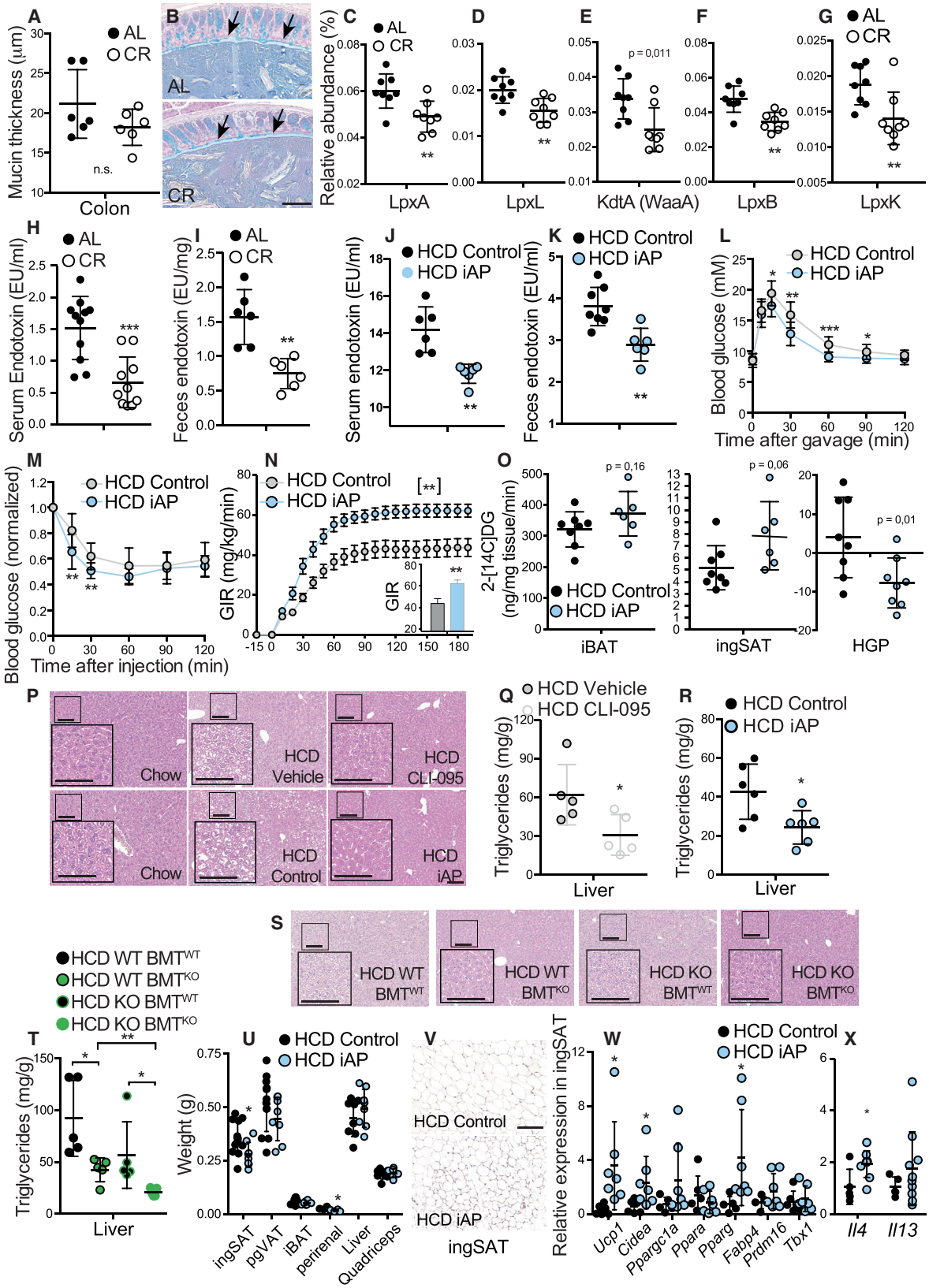

(legend on next page)

compared with HCD-fed controls (Figures 7P–7R, S7M, and S7N), while the *Tlr4*$^{-/-}$ BMT experiments showed that the suppressed LPS-TLR4 signaling in both BM cells and hepatocytes contributed to the reduced HCD-driven liver fat accumulation (Figures 7S, 7T, and S7O). Finally, despite the increased glucose uptake, the ingSAT was smaller in size and had smaller multilocular adipocytes (Figures 7U and 7V), suggesting that iAP promotes browning. Accordingly, the ingSAT of the iAP-treated mice showed enhanced expression of the type 2 cytokines and browning markers (Figures 7V and 7W). Together, these data demonstrate that CR-induced gut microbiota alterations suppress lipid A and LPS biosynthesis, leading to fat browning and a number of systemic metabolic improvements.

DISCUSSION

The weight loss during CR occurs due to the negative energy balance and is potentiated by the fat browning (Fabbiano et al., 2016). The microbiota alteration during CR dictates the tone of the immune response and contributes to the increased browning, fat loss, and many of the metabolic improvements seen during CR. Interestingly, microbiota-depleted WT and GF mice treated with antibiotics show limited responsiveness to CR, further pointing to the importance of the CR-induced microbiota alterations in contributing to the overall metabolic benefits of the CR. Consistent with the innate immunity-mediated CR-induced browning, the *Tlr4* KO bone marrow-derived hematopoietic cells increase beige fat development in recipient mice irrespective of their genetic background, while *Tlr4* KO mice are resistant to further improvements of their metabolic status during CR.

These results provide a possible direct link between the functional microbiota changes, the immune system, and the fat metabolism, and suggest several strategies to promote beige fat development and improve metabolic outcome. On one hand, the CR microbiota alone is sufficient to enhance insulin sensitivity, improve tolerance to glucose and cold, and reduce fat content, and this effect is at least in part mediated by browning of the white fat depots. In line with this, fecal microbiota transplantation (Eiseman et al., 1958) has regained interest as a treatment option for several pathologies (Khoruts, 2014). On the other hand, the translational importance of our study can be further exploited by modulating the mechanism by which CR microbiota promotes browning. Pharmacological treatment with a TLR4 antagonist phenocopied a number of CR-induced metabolic improvements and induced browning. Similarly, mimicking the CR-microbiota changes by detoxifying LPS through iAP oral supplementation enhanced beige fat development. Both treatments reduced fatty liver progression during HCD, which was mediated by LPS-TLR4 signaling in both hematopoietic cells and hepatocytes. Together, these data suggest a molecular explanation of the microbiota-immune system-fat signaling axis, and imply the microbiota as a key player mediating the metabolic benefits of CR with large therapeutic potential.

Limitations of the Study

Our study shows that the LPS decrease during CR in lean mice is linked to changes in the rate-limiting enzymes necessary for the lipid A biosynthesis; however, additional data would be needed to formally conclude this link. While the decreased LPS levels in both plasma and feces indeed suggest that the LPS biosynthesis is reduced during CR and iAP treatment, we can't exclude that the alterations in the intestinal function after CR below the detection limit, or after the genetic and pharmacological inhibition of TLR4 during HCD feeding could contribute to the effects. We demonstrate that the microbiota alterations during CR are sufficient to promote the fat browning and the improved glycemic control. This does not rule out that additional mechanisms operate to further regulate these processes during CR. Finally, the BMT experiments do not allow discrimination of the bone marrow-derived cell populations that are mediating the effects following TLR4 inhibition and after CR, and additional specific mouse line experiments would be needed to further narrow this down. We hope that our future work will provide a deeper understanding of the molecular changes in the immune cells underlying the CR-induced browning.

STAR★METHODS

Detailed methods are provided in the online version of this paper and include the following:

- KEY RESOURCES TABLE
- CONTACT FOR REAGENT AND RESOURCE SHARING

Figure 7. iAP Induces Browning and Improves Metabolic Health During HCD

(A and B) Colon mucin layer thickness quantification (A) and representative Alcian blue-stained (arrows) sections (B) of AL and CR mice (n = 6 per group). Scale bar, 200 μm.

(C–G) Relative abundance of LpxA (C), LpxL (D), KdtA (E), LpxB (F), and LpxK (G) involved in lipid A biosynthesis detected by metagenomics analysis as level 4 functions in fecal samples from AL and CR mice (n = 8 per group).

(H and I) Endotoxin levels in serum (H) and feces (I) of AL and CR mice determined by limulus amebocyte lysate (LAL) colorimetric assay (n = 6–11 per group).

(J and K) Endotoxin levels in serum (J) and feces (K) of HCD-fed control and iAP mice determined by LAL colorimetric assay (n = 6–8 per group).

(L and M) OGTT (L) and ITT (M) of HCD control and iAP mice (n = 12 per group).

(N and O) Glucose infusion rate (N) and 2-[^{14}C]DG uptake (O) in indicated tissues during hyperinsulinemic-euglycemic clamp. Error bars show mean ± SEM (n = 8).

(P) Representative H&E-stained histological sections from livers of the indicated mice. Scale bars, 100 μm.

(Q and R) Liver triglyceride content in HCD vehicle and CLI-095 (Q) of control and iAP (R) mice.

(S) Representative H&E-stained histological sections from livers of the indicated BMT mice. Scale bars, 100 μm.

(T) Liver triglyceride content in HCD BMT mice (e).

(U) Weight of indicated organs post mortem of HCD control and iAP mice (n = 12).

(V) Representative H&E-stained histological sections from ingSAT of HCD control and iAP mice. Scale bar, 200 μm.

(W and X) Relative mRNA expression of browning markers (W) and type 2 cytokines (X) in ingSAT of HCD control and iAP mice (n = 6).

Unless otherwise indicated, error bars show mean ± SD. Significance was calculated using non-paired two-tailed Student's t test. *$p \leq 0.05$, **$p \leq 0.01$, ***$p \leq 0.001$; n.s., not significant.

SUPPLEMENTAL INFORMATION

Supplemental Information includes seven figures and can be found with this article online at https://doi.org/10.1016/j.cmet.2018.08.005.

ACKNOWLEDGMENTS

We thank Maria Josephine Gustafsson Trajkovska, Claes Wollheim, and all members of the Trajkovski lab for discussions and critical reading of the manuscript; Didier Colin for help with the PET-CT; Myriam Girard for help with PCR amplification of the 16S rRNA; and Xosé R. Bustelo for kindly providing the C57BL/10 mice. S.F. was supported by a postdoctoral fellowship of the Peter und Traudl Engelhorn Stiftung. The research leading to these results has received funding from the European Research Council under the European Union's Seventh Framework Program (FP/2007-2013)/ERC grant agreement no. 336607 (ERC-2013-StG-336607), the Clayton Foundation, the Louis-Jeantet Foundation, and the Swiss National Science Foundation Professorship to M.T.

AUTHOR CONTRIBUTIONS

S.F. designed and performed the experiments, developed the hypothesis, analyzed data, and prepared figures; N.S.-Z., C.C., D.R., and C.V.-D. participated in experiments; S.K., S.L., C.C., N.G., V.L., and J.S. carried out the 16S and the metagenomic sequencing and analysis; M.M. advised and provided the iAP; D.M. obtained the *Tlr4* KO mice and information from SwImMR; M.G.d.A. and A.M. provided the GF mice; M.T. initiated, designed, and supervised the work, developed the hypothesis, and analyzed data; S.F. and M.T. wrote the manuscript with input from all co-authors.

DECLARATION OF INTERESTS

The authors declare no competing interests.

Received: June 1, 2018
Revised: July 13, 2018
Accepted: August 2, 2018
Published: August 30, 2018

REFERENCES

Backhed, F., Ding, H., Wang, T., Hooper, L.V., Koh, G.Y., Nagy, A., Semenkovich, C.F., and Gordon, J.I. (2004). The gut microbiota as an environmental factor that regulates fat storage. Proc. Natl. Acad. Sci. USA *101*, 15718–15723.

Barzilai, N., Banerjee, S., Hawkins, M., Chen, W., and Rossetti, L. (1998). Caloric restriction reverses hepatic insulin resistance in aging rats by decreasing visceral fat. J. Clin. Invest. *101*, 1353–1361.

Barzilai, N., and Gabriely, I. (2001). The role of fat depletion in the biological benefits of caloric restriction. J. Nutr. *131*, 903S–906S.

Bentala, H., Verweij, W.R., Huizinga-Van der Vlag, A., van Loenen-Weemaes, A.M., Meijer, D.K., and Poelstra, K. (2002). Removal of phosphate from lipid A as a strategy to detoxify lipopolysaccharide. Shock *18*, 561–566.

Bolger, A.M., Lohse, M., and Usadel, B. (2014). Trimmomatic: a flexible trimmer for Illumina sequence data. Bioinformatics *30*, 2114–2120.

Buchfink, B., Xie, C., and Huson, D.H. (2015). Fast and sensitive protein alignment using DIAMOND. Nat. Methods *12*, 59–60.

Camell, C.D., Sander, J., Spadaro, O., Lee, A., Nguyen, K.Y., Wing, A., Goldberg, E.L., Youm, Y.H., Brown, C.W., Elsworth, J., et al. (2017). Inflammasome-driven catecholamine catabolism in macrophages blunts lipolysis during ageing. Nature *550*, 119–123.

Cani, P.D., Amar, J., Iglesias, M.A., Poggi, M., Knauf, C., Bastelica, D., Neyrinck, A.M., Fava, F., Tuohy, K.M., Chabo, C., et al. (2007). Metabolic endotoxemia initiates obesity and insulin resistance. Diabetes *56*, 1761–1772.

Canto, C., and Auwerx, J. (2011). Calorie restriction: is AMPK a key sensor and effector? Physiology *26*, 214–224.

Caporaso, J.G., Lauber, C.L., Walters, W.A., Berg-Lyons, D., Lozupone, C.A., Turnbaugh, P.J., Fierer, N., and Knight, R. (2011). Global patterns of 16S rRNA diversity at a depth of millions of sequences per sample. Proc. Natl. Acad. Sci. USA *108* (*Suppl 1*), 4516–4522.

Chen, K.T., Malo, M.S., Moss, A.K., Zeller, S., Johnson, P., Ebrahimi, F., Mostafa, G., Alam, S.N., Ramasamy, S., Warren, H.S., et al. (2010). Identification of specific targets for the gut mucosal defense factor intestinal alkaline phosphatase. Am. J. Physiol. Gastrointest. Liver Physiol. *299*, G467–G475.

Chevalier, C., Stojanovic, O., Colin, D.J., Suarez-Zamorano, N., Tarallo, V., Veyrat-Durebex, C., Rigo, D., Fabbiano, S., Stevanovic, A., Hagemann, S., et al. (2015). Gut microbiota orchestrates energy homeostasis during cold. Cell *163*, 1360–1374.

Chung, K.J., Chatzigeorgiou, A., Economopoulou, M., Garcia-Martin, R., Alexaki, V.I., Mitroulis, I., Nati, M., Gebler, J., Ziemssen, T., Goelz, S.E., et al. (2017). A self-sustained loop of inflammation-driven inhibition of beige adipogenesis in obesity. Nat. Immunol. *18*, 654–664.

Dao, M.C., Everard, A., Aron-Wisnewsky, J., Sokolovska, N., Prifti, E., Verger, E.O., Kayser, B.D., Levenez, F., Chilloux, J., Hoyles, L., et al. (2015). Akkermansia muciniphila and improved metabolic health during a dietary intervention in obesity: relationship with gut microbiome richness and ecology. Gut *65*, 426–436.

De Guzman, J.M., Ku, G., Fahey, R., Youm, Y.H., Kass, I., Ingram, D.K., Dixit, V.D., and Kheterpal, I. (2013). Chronic caloric restriction partially protects against age-related alteration in serum metabolome. Age *35*, 1091–1104.

Desai, M.S., Seekatz, A.M., Koropatkin, N.M., Kamada, N., Hickey, C.A., Wolter, M., Pudlo, N.A., Kitamoto, S., Terrapon, N., Muller, A., et al. (2016). A dietary fiber-deprived gut microbiota degrades the colonic mucus barrier and enhances pathogen susceptibility. Cell *167*, 1339–1353.e21.

Desai, T.A., and Rao, C.V. (2010). Regulation of arabinose and xylose metabolism in Escherichia coli. Appl. Environ. Microbiol. *76*, 1524–1532.

Edgar, R.C. (2013). UPARSE: highly accurate OTU sequences from microbial amplicon reads. Nat. Methods *10*, 996–998.

Eiseman, B., Silen, W., Bascom, G.S., and Kauvar, A.J. (1958). Fecal enema as an adjunct in the treatment of pseudomembranous enterocolitis. Surgery *44*, 854–859.

Emiola, A., George, J., and Andrews, S.S. (2014). A complete pathway model for lipid a biosynthesis in *Escherichia coli*. PLoS One *10*, e0121216.

Everard, A., Lazarevic, V., Gaia, N., Johansson, M., Stahlman, M., Backhed, F., Delzenne, N.M., Schrenzel, J., Francois, P., and Cani, P.D. (2014). Microbiome of prebiotic-treated mice reveals novel targets involved in host response during obesity. ISME J. *8*, 2116–2130.

Fabbiano, S., Suarez-Zamorano, N., Rigo, D., Veyrat-Durebex, C., Stevanovic Dokic, A., Colin, D.J., and Trajkovski, M. (2016). Caloric restriction leads to browning of white adipose tissue through type 2 immune signaling. Cell Metab. *24*, 434–446.

Fabbiano, S., Suarez-Zamorano, N., and Trajkovski, M. (2017). Host-microbiota mutualism in metabolic diseases. Front. Endocrinol. (Lausanne) *8*, 267.

Feldmann, H.M., Golozoubova, V., Cannon, B., and Nedergaard, J. (2009). UCP1 ablation induces obesity and abolishes diet-induced thermogenesis in mice exempt from thermal stress by living at thermoneutrality. Cell Metab. *9*, 203–209.

Fischer, K., Ruiz, H.H., Jhun, K., Finan, B., Oberlin, D.J., van der Heide, V., Kalinovich, A.V., Petrovic, N., Wolf, Y., Clemmensen, C., et al. (2017). Alternatively activated macrophages do not synthesize catecholamines or contribute to adipose tissue adaptive thermogenesis. Nat. Med. *23*, 623–630.

Griffin, N.W., Ahern, P.P., Cheng, J., Heath, A.C., Ilkayeva, O., Newgard, C.B., Fontana, L., and Gordon, J.I. (2017). Prior dietary practices and connections to a human gut microbial metacommunity alter responses to diet interventions. Cell Host Microbe *21*, 84–96.

Herlemann, D.P., Labrenz, M., Jurgens, K., Bertilsson, S., Waniek, J.J., and Andersson, A.F. (2011). Transitions in bacterial communities along the 2000 km salinity gradient of the baltic sea. ISME J. *5*, 1571–1579.

Jia, L., Vianna, C.R., Fukuda, M., Berglund, E.D., Liu, C., Tao, C., Sun, K., Liu, T., Harper, M.J., Lee, C.E., et al. (2014). Hepatocyte Toll-like receptor 4 regulates obesity-induced inflammation and insulin resistance. Nat. Commun. *5*, 3878.

Kaliannan, K., Hamarneh, S.R., Economopoulos, K.P., Nasrin Alam, S., Moaven, O., Patel, P., Malo, N.S., Ray, M., Abtahi, S.M., Muhammad, N., et al. (2013). Intestinal alkaline phosphatase prevents metabolic syndrome in mice. Proc. Natl. Acad. Sci. USA *110*, 7003–7008.

Kelley, D.E., Wing, R., Buonocore, C., Sturis, J., Polonsky, K., and Fitzsimmons, M. (1993). Relative effects of calorie restriction and weight loss in noninsulin-dependent diabetes mellitus. J. Clin. Endocrinol. Metab. *77*, 1287–1293.

Khoruts, A. (2014). Faecal microbiota transplantation in 2013: developing human gut microbiota as a class of therapeutics. Nat. Rev. Gastroenterol. Hepatol. *11*, 79–80.

Kim, K.A., Gu, W., Lee, I.A., Joh, E.H., and Kim, D.H. (2012). High fat diet-induced gut microbiota exacerbates inflammation and obesity in mice via the TLR4 signaling pathway. PLoS One *7*, e47713.

Koren, O., Goodrich, J.K., Cullender, T.C., Spor, A., Laitinen, K., Backhed, H.K., Gonzalez, A., Werner, J.J., Angenent, L.T., Knight, R., et al. (2012). Host remodeling of the gut microbiome and metabolic changes during pregnancy. Cell *150*, 470–480.

Kumari, M., Wang, X., Lantier, L., Lyubetskaya, A., Eguchi, J., Kang, S., Tenen, D., Roh, H.C., Kong, X., Kazak, L., et al. (2016). IRF3 promotes adipose inflammation and insulin resistance and represses browning. J. Clin. Invest. *126*, 2839–2854.

Li, G., Xie, C., Lu, S., Nichols, R.G., Tian, Y., Li, L., Patel, D., Ma, Y., Brocker, C.N., Yan, T., et al. (2017). Intermittent fasting promotes white adipose browning and decreases obesity by shaping the gut microbiota. Cell Metab. *26*, 672–685.e4.

Liou, A.P., Paziuk, M., Luevano, J.M., Jr., Machineni, S., Turnbaugh, P.J., and Kaplan, L.M. (2013). Conserved shifts in the gut microbiota due to gastric bypass reduce host weight and adiposity. Sci. Transl. Med. *5*, 178ra141.

Louis, S., Tappu, R.M., Damms-Machado, A., Huson, D.H., and Bischoff, S.C. (2016). Characterization of the gut microbial community of obese patients following a weight-loss intervention using whole metagenome shotgun sequencing. PLoS One *11*, e0149564.

Nguyen, K.D., Qiu, Y., Cui, X., Goh, Y.P., Mwangi, J., David, T., Mukundan, L., Brombacher, F., Locksley, R.M., and Chawla, A. (2011). Alternatively activated macrophages produce catecholamines to sustain adaptive thermogenesis. Nature *480*, 104–108.

Ocampo, A., Liu, J., Schroeder, E.A., Shadel, G.S., and Barrientos, A. (2012). Mitochondrial respiratory thresholds regulate yeast chronological life span and its extension by caloric restriction. Cell Metab. *16*, 55–67.

Okla, M., Wang, W., Kang, I., Pashaj, A., Carr, T., and Chung, S. (2015). Activation of Toll-like receptor 4 (TLR4) attenuates adaptive thermogenesis via endoplasmic reticulum stress. J. Biol. Chem. *290*, 26476–26490.

Ott, B., Skurk, T., Hastreiter, L., Lagkouvardos, I., Fischer, S., Buttner, J., Kellerer, T., Clavel, T., Rychlik, M., Haller, D., et al. (2017). Effect of caloric restriction on gut permeability, inflammation markers, and fecal microbiota in obese women. Sci. Rep. *7*, 11955.

Overbeek, R., Begley, T., Butler, R.M., Choudhuri, J.V., Chuang, H.Y., Cohoon, M., de Crecy-Lagard, V., Diaz, N., Disz, T., Edwards, R., et al. (2005). The subsystems approach to genome annotation and its use in the project to annotate 1000 genomes. Nucleic Acids Res. *33*, 5691–5702.

Pirzgalska, R.M., Seixas, E., Seidman, J.S., Link, V.M., Sanchez, N.M., Mahu, I., Mendes, R., Gres, V., Kubasova, N., Morris, I., et al. (2017). Sympathetic neuron-associated macrophages contribute to obesity by importing and metabolizing norepinephrine. Nat. Med. *23*, 1309–1318.

Pruesse, E., Quast, C., Knittel, K., Fuchs, B.M., Ludwig, W., Peplies, J., and Glockner, F.O. (2007). SILVA: a comprehensive online resource for quality checked and aligned ribosomal RNA sequence data compatible with ARB. Nucleic Acids Res. *35*, 7188–7196.

Qiu, Y., Nguyen, K.D., Odegaard, J.I., Cui, X., Tian, X., Locksley, R.M., Palmiter, R.D., and Chawla, A. (2014). Eosinophils and type 2 cytokine signaling in macrophages orchestrate development of functional beige fat. Cell *157*, 1292–1308.

Razolli, D.S., Moraes, J.C., Morari, J., Moura, R.F., Vinolo, M.A., and Velloso, L.A. (2015). TLR4 expression in bone marrow-derived cells is both necessary and sufficient to produce the insulin resistance phenotype in diet-induced obesity. Endocrinology *156*, 103–113.

Ridaura, V.K., Faith, J.J., Rey, F.E., Cheng, J., Duncan, A.E., Kau, A.L., Griffin, N.W., Lombard, V., Henrissat, B., Bain, J.R., et al. (2013). Gut microbiota from twins discordant for obesity modulate metabolism in mice. Science *341*, 1241214.

Schmieder, R., and Edwards, R. (2011). Fast identification and removal of sequence contamination from genomic and metagenomic datasets. PLoS One *6*, e17288.

Schneeberger, M., Everard, A., Gomez-Valades, A.G., Matamoros, S., Ramirez, S., Delzenne, N.M., Gomis, R., Claret, M., and Cani, P.D. (2015). Akkermansia muciniphila inversely correlates with the onset of inflammation, altered adipose tissue metabolism and metabolic disorders during obesity in mice. Sci. Rep. *5*, 16643.

Sekirov, I., Russell, S.L., Antunes, L.C., and Finlay, B.B. (2010). Gut microbiota in health and disease. Physiol. Rev. *90*, 859–904.

Silva, G.G.Z., Green, K.T., Dutilh, B.E., and Edwards, R.A. (2016). SUPER-FOCUS: a tool for agile functional analysis of shotgun metagenomic data. Bioinformatics *32*, 354–361.

Spiljar, M., Merkler, D., and Trajkovski, M. (2017). The immune system bridges the gut microbiota with systemic energy homeostasis: focus on TLRs, mucosal barrier, and SCFAs. Front. Immunol. *8*, 1353.

Suarez-Zamorano, N., Fabbiano, S., Chevalier, C., Stojanovic, O., Colin, D.J., Stevanovic, A., Veyrat-Durebex, C., Tarallo, V., Rigo, D., Germain, S., et al.

(2015). Microbiota depletion promotes browning of white adipose tissue and reduces obesity. Nat. Med. *21*, 1497–1501.

Sun, L., and Trajkovski, M. (2014). MiR-27 orchestrates the transcriptional regulation of brown adipogenesis. Metabolism *63*, 272–282.

Thaiss, C.A., Itav, S., Rothschild, D., Meijer, M., Levy, M., Moresi, C., Dohnalova, L., Braverman, S., Rozin, S., Malitsky, S., et al. (2016). Persistent microbiome alterations modulate the rate of post-dieting weight regain. Nature *540*, 544–551.

Trajkovski, M., Ahmed, K., Esau, C.C., and Stoffel, M. (2012). MyomiR-133 regulates brown fat differentiation through Prdm16. Nat. Cell Biol. *14*, 1330–1335.

Turnbaugh, P.J., Hamady, M., Yatsunenko, T., Cantarel, B.L., Duncan, A., Ley, R.E., Sogin, M.L., Jones, W.J., Roe, B.A., Affourtit, J.P., et al. (2009). A core gut microbiome in obese and lean twins. Nature *457*, 480–484.

Turnbaugh, P.J., Ley, R.E., Mahowald, M.A., Magrini, V., Mardis, E.R., and Gordon, J.I. (2006). An obesity-associated gut microbiome with increased capacity for energy harvest. Nature *444*, 1027–1031.

Wang, X., and Quinn, P.J. (2010). Lipopolysaccharide: biosynthetic pathway and structure modification. Prog. Lipid Res. *49*, 97–107.

Zhang, C., Li, S., Yang, L., Huang, P., Li, W., Wang, S., Zhao, G., Zhang, M., Pang, X., Yan, Z., et al. (2013). Structural modulation of gut microbiota in life-long calorie-restricted mice. Nat. Commun. *4*, 2163.

Zhang, J., Kobert, K., Flouri, T., and Stamatakis, A. (2014). PEAR: a fast and accurate Illumina paired-end reAd mergeR. Bioinformatics *30*, 614–620.

Zhang, N., Liang, H., Farese, R.V., Li, J., Musi, N., and Hussey, S.E. (2015). Pharmacological TLR4 inhibition protects against acute and chronic fat-induced insulin resistance in rats. PLoS One *10*, e0132575.

STAR★METHODS

KEY RESOURCES TABLE

REAGENT or RESOURCE	SOURCE	IDENTIFIER
Antibodies		
Anti-UCP1	Pierce Antibodies	PA1-24894
Anti-F4/80	Abcam	Clone A3-1, cat # ab105155
Anti-CD11b	BD Biosciences	Clone M1/70, cat # 561114
Anti-CD301	BioLegend	Clone LOM-14, cat # 145705
Anti-CD45	BD Biosciences	Clone 104, cat #558702
Anti-Siglec F	BD Biosciences	Clone E50-2440, cat # 562068
Goat anti-Rat IgG (H+L) Secondary Antibody, Alexa Fluor 488 conjugate	Thermo Fisher Scientific	A-11006
Chemicals, Peptides, and Recombinant Proteins		
Lipopolysaccharides from *Escherichia coli* 0127:B8	Sigma Aldrich	L3129 -100MG
CLI-095	Invivogen	tlrl-cli95
Intestinal alkaline phosphatase from bovine intestinal mucosa	Sigma Aldrich	P0114
Dextran-FITC	Sigma-Aldrich	Ref. 46944-500MG-F
Trizol	Life Technologies; Manufacturer: Thermo Scientific	15596018
RNAlater Stabilization Solution	Thermo Fisher Scientific	AM7020
Critical Commercial Assays		
LAL Chromogenic Endotoxin Quantitation Kit	Thermo Fisher Scientific	88282
Endosafe PTS cartridges	Charles River Microbial Solutions	PTS55005F
Serum Triglyceride Determination Kit	Sigma Aldrich	TR0100-1KT
Mouse Insulin ELISA Kit	Mercodia	10-1247-01
QIAmp Fast DNA Stool Mini Kit	Qiagen	51604
PowerFecal DNA Kit	Qiagen	12830-50
qPCR SYBR Green Power	Thermo Fisher Scientific	A25778
Deposited Data		
Reference for the metagenomics and 16S rDNA data	NCBI short read archive (SRA)	SRA: PRJNA480387
Experimental Models: Organisms/Strains		
C57BL/6J mice	Charles River	000664
C57BL/6 Germ-Free mice	Clean animal facility, University of Bern	N/A
B6.B10ScN-*Tlr4*$^{lps\text{-}del}$/JthJ	Charles River	007227
C57BL/6J CD45.1 (Ly5.1)+ mice	Charles River	002014
C57BL/10J mice	Jackson Laboratories, and Prof. X.R. Bustelo, Salamanca, Spain	000665
C57BL/10ScNJ	SwImMR consortium	N/A
Oligonucleotides		
Name	Forward Primer	Reverse Primer
M. musculus Ucp1	5′-GGCCTCTACGACTCAGTCCA-3′	5′-TAAGCCGGCTGAGATCTTGT-3′
M. musculus Cidea	5′-TGCTCTTCTGTATCGCCCAGT-3′	5′-GCCGTGTTAAGGAATCTGCTG-3′
M. musculus Ppargc1a	5′-AAGTGTGGAACTCTCTGGAACTG-3′	5′-GGGTTATCTTGGTTGGCTTTATG-3′
M. musculus Ppara	5′-AGAGCCCCATCTGTCCTCTC-3′	5′-ACTGGTAGTCTGCAAAACCAAA-3′
M. musculus Pparg	5′-AGGCGAGGGCGATCTTGACAG-3′	5′-AATTCGGATGGCCACCTCTTTG-3′
M. musculus Prdm16	5′-CAGCACGGTGAAGCCATT-3′	5′-GCGTGCATCCGCTTGTG-3′

(*Continued on next page*)

Continued		
REAGENT or RESOURCE	SOURCE	IDENTIFIER
M. musculus Tbx1	5′-GGCAGGCAGACGAATGTTC-3′	5′-TTGTCATCTACGGGCACAAAG-3′
M. musculus Fabp4	5′-ACACCGAGTTTCCTTCAAACTG-3′	5′-CCATCTAGGGTTATGATGCTCTTCA-3′
M. musculus Th	5′-GGTATACGCCACGCTGAAGG-3′	5′-TAGCCACAGTACCGTTCCAGA-3′
M. musculus Il4	5′-GGTCTCAACCCCCAGCTAGT-3′	5′-GCCGATGATCTCTCTCAAGTGAT-3′
M. musculus Il13	5′-CCTGGCTCTTGCTTGCCTT-3′	5′-GGTCTTGTGTGATGTTGCTCA-3′
M. musculus Myd88	5′-TGCCGTCCTGTCTACATCTTTG-3′	5′-GTTGCTCAGGCCAGTCATCA-3′
M. musculus Lbp	5′-CTCTACCCTGATGTCAATGCTG-3′	5′-GAGGTCGTGGAGCTGAATATG-3′
M. musculus Intectin	5′-GTTGCCCCTGATTCTGCTGG-3′	5′-GCACTATTGCAGAGGTCCGT-3′
Species - Akkermansia Muciniphila - 16SrRNA gene	5′-CAGCACGTGAAGGTGGGGAC-3′	5′-CCTTGCGGTTGGCTTCAGAT-3′
16S rRNA gene across V4-V5 variable regions	5′-CAGCAGCCGCGGTAATAC-3′	5′-CCGTCAATTCCTTTGAGTTT-3′
16S rRNA gene V4 variable region (515F- 806R)	5′-GTGCCAGCMGCCGCGGTAA-3′	5′-GGACTACHVGGGTWTCTAAT-3′
Phylum- Firmicutes - 16SrRNA gene	5′-CTGATGGAGCAACGCCGCGT-3′	5′-ACACYTAGYACTCATCGTTT-3′
Phylum- Bacteroidetes - 16SrRNA gene	5′-CCGGAWTYATTGGGTTTAAAGGG-3′	5′-GGTAAGGTTCCTCGCGTA-3′
Phylum- Actinobacteria - 16SrRNA gene	5′-GCGKCCTATCAGCTTGTT-3′	5′-CCGCCTACGAGCYCTTTACGC-3′
Class-β and γ proteobacteria - 16SrRNA gene	5′-GTATAATGGGTCAGCGAC-3′	5′-TTACCGCGGCTGCTGGCAC-3′
Software and Algorithms		
Qiime		V1.9.1
SILVA Incremental Aligner	Pruesse et al., 2007	v1.2.11
SUPER-FOCUS	Silva et al., 2016	
DECONSEQ	Schmieder and Edwards, 2011	
Other		
Mini-osmotic pumps	Alzet	2004
Greengenes	greengenes.secondgenome.com	v13.8
SEED database	Overbeek et al., 2005	
Countour XT NEXT strips	Ascencia	CONTOUR NEXT Strips CONTOUR

CONTACT FOR REAGENT AND RESOURCE SHARING

Further information and requests for resources and reagents should be directed to and will be fulfilled by the Lead Contact, Mirko Trajkovski (mirko.trajkovski@unige.ch).

EXPERIMENTAL MODEL AND SUBJECT DETAILS

Animals

Cd45.1+ (B6.SJL-Ptprca Pepcb/BoyJ, The Jackson Laboratory (Jax) Stock #002014), *Tlr4* KO (B6.B10ScN-Tlr4lps-del/JthJ, Jax Stock #007227; *Tlr4*$^{-/-}$) mice and their C57BL/6J controls (WT, Jax Stock #000664) were originally purchased through Charles River. Germ-free (GF) mice on C57BL/6 background were obtained from the Germ-Free (Clean animal) facility at the University of Bern. The experiments addressing the CR metabolic effects were reproduced in C57BL/6JRj (Janvier); as well as in *Tlr4* KO mice on C57BL/10J background (C57BL/10ScNJ) obtained through the Swiss Immune Mouse Repository (SwImMR) consortium (Zurich, Switzerland), and C57BL/10J control mice (obtained through Charles River (Jax Stock #000665), or provided by Prof. Xosé R. Bustelo, University of Salamanca) to confirm the findings (not shown). Mice were kept in a specific pathogen free facility (SPF) in 12 hr day and night cycles and were fed either standard chow diet (16.2 MJ/kg Gross Energy; 9 kJ% Fat, 33 kJ% Protein, 58 kJ% Carbohydrates, V1534-727, Ssniff, Germany) high-fat, high-sugar diet (HCD), (22.1 MJ/kg Gross Energy; 45 kJ% Fat, 20 kJ% Protein, 35 kJ% Carbohydrates, D12451, Ssniff, Germany) or 60% calorie restricted diet (low caloric diet, LCD) (14.6 MJ/kg Gross Energy; 7.7 MJ/kg Metabolizable Energy; 11 kJ% Fat, 51 kJ% Protein, 38 kJ% Carbohydrates, S9631-S710, Ssniff, Germany). Animals under caloric restriction were fed daily with 40% less standard chow diet food than the average eaten by age-matched *ad libitum* fed mice, and food was provided each day at 18 hr. Cold exposures were performed at 6°C in a light and humidity controlled climatic chamber (TSE, Germany) in SPF conditions. Antibiotics (Abx), where indicated, were administered in the drinking water *ad libitum* and replaced with freshly prepared cocktails every second day containing 100 μg/mL Neomycin, 50 μg/mL Streptomycin, 100 U/mL Penicillin, 50 μg/mL Vancomycin, 100 μg/mL Metronidazole, 1 mg/mL Bacitracin, 125 μg/mL Ciprofloxacin, 100 μg/mL Ceftazidime (Sigma, Germany; Alkaloid, Macedonia). All experiments were started on male, 8-week-old mice, unless otherwise stated. Upon arrival or

after weaning, animals were allocated to groups based on their body weight to ensure equal starting points. All mice were sacrificed after 5 hr fasting. 500 μL of blood was taken from terminally anesthetized mice in tubes with 11 μL of 0.5 mM EDTA, 2 μL of aprotinin and 2 μL of DPPIV and plasma stored at −80°C. All animal experiments were approved by the Swiss federal and Geneva cantonal authorities for animal experimentation (Office vétérinaire federal and Comission cantonale pour les expériences sur les animaux de Genève).

METHOD DETAILS

Bacterial 16S Sequencing

These analyses were performed in two independent cohorts of mice and using different sets of techniques. For the first cohort, feces and cecum DNA was extracted using the QIAmp Fast DNA Stool Mini Kit (Qiagen). Two negative extraction controls were performed by substituting the stool samples with water in the extraction procedure. DNA concentration in the extracts was measured using a Qubit dsDNA BR Assay Kit on a Qubit 2.0 Fluorometer (*Life Technologies*, Carlsbad, California, USA). The V3-4 region of the bacterial 16S rRNA genes (E. coli positions 341-805) was amplified using 1 μL of DNA extract adjusted to 1 ng/μL for samples (undiluted for negative extraction controls) in a 25 μL volume that contained 12.5 μL KAPA2G Robust HotStart ReadyMix (Kapa Biosystems, Boston, MA, USA) and 0.5 μL each of 10 μM forward primer 341F 5′-CCTACGGGNGGCWGCAG-3′ and reverse primer 805R 5′-GAC TACHVGGGTATCTAAKCC-3′ (Herlemann et al., 2011). The reverse primer contained an additional ambiguous base in comparison to the original sequence. The PCR conditions included an initial denaturation at 95°C for 3 min, followed by 30 cycles of denaturation at 95°C for 30 s, annealing at 51°C for 30 s, and extension at 72°C for 30 s, with a final extension at 72°C for 5 min. Each PCR was performed in triplicate and the products were combined. The pooled sample was run on a 2100 Bioanalyzer (Agilent Technologies, Santa Clara, CA) for quality analysis and quantification. The primers from the first round of PCR were removed by digesting 5 μL samples (containing 9.5-13.9 ng/μL DNA except in negative extraction controls for which DNA concentration was under the detection level) with 1 unit Exonuclease I (New England Biolabs, Ipswich, MA, USA) in a total volume of 10 μL Exonuclease I Reaction Buffer (New England Biolabs) at 37°C for 30 min. The enzyme was inactivated at 95°C for 15 min. Amplicon barcoding was performed by re-amplification using 1 μL of Exonuclease I-treated first-round PCR, 15 pmol each of forward primer 5′-NNNNNNNNNNTCCTA CGGGNGGCWGCAG-3′ and reverse primer 5′- NNNNNNNNNNTGACTACHVGGGTATCTAAKCC-3′ in a 20-μL volume of MyTaq buffer that contained 1.5 units MyTaq DNA polymerase (Bioline, London, UK) and 2 μL of BioStab PCR optimizer (II) (Sigma-Aldrich, Munich, Germany). For each sample, the forward and reverse primers had the same 10-nt barcode sequence. PCRs were carried out using the following parameters: pre-denaturation for 2 min at 96°C, followed by eight cycles of 96°C for 15 s, 50°C for 30 s, and 70°C for 90 s. DNA concentration of amplicons of interest was determined by gel electrophoresis. About 20 ng amplicon DNA of each sample were pooled (or a 2 μL solution for negative extraction controls) and purified with one volume Agencourt AMPure XP beads (Beckman Coulter, Nyon, Switzerland) to remove primer dimers and other small mispriming products, followed by an additional purification using a MinElute PCR Purification Kit (Qiagen, Venlo, the Netherlands). About 100 ng of the pooled amplicon DNA was used to construct a sequencing library using the Ovation Rapid DR Multiplex System 1-96 (NuGEN, San Carlos, CA, USA). The library was size-selected by gel electrophoresis and sequenced from both ends for 300 cycles on the Illumina MiSeq using MiSeq v3 Reagent Kit (Illumina, San Diego, CA, USA) at LGC Genomics (Berlin, Germany). Demultiplexed FASTQ files were generated from base-calls using Illumina's bcl2fastq v1.8.4 software. Reads with incorrect barcodes, missing barcodes, or conflicting barcode pairs were discarded. Adapter remnants and primer sequences were removed using proprietary LGC Genomics software. Paired reads were quality filtered and joined using PEAR v0.9.6 (Zhang et al., 2014) with the following parameters: -m 450 -n 390 -v 50 -q 33 -t 250 -p 0.0001 -u 0. Merged sequence reads (fastq format) were processed using the default UPARSE v8.1.64 pipeline (Edgar, 2013) that clusters reads into operational taxonomic units (OTUs) at the 97% similarity threshold. Maximum expected error threshold (-fastq_maxee E) was set at 1. Representative sequence of each OTU was classified using the online SILVA Incremental Aligner (SINA) v1.2.11 (Pruesse et al., 2007) with default settings and SILVA taxonomy for classification. Twenty OTUs that did not fit the following criteria: start at positions 6,425-6,427 (positions 357-358 in *Escherichia coli* 16S rRNA gene), end in the 23,439-23,442 range and present >80% identity with the SILVA SSU SEED alignment sequences were excluded. Eleven OTUs with mean relative abundance >0.1% in the negative extraction controls were removed from the sample data set. The number of reads per sample was rarefied to 22,504 (lowest count in any sample).

For the second cohort, bacterial DNA content was extracted using PowerFecal DNA Kit (Qiagen, Ref. 12830-50) and PCR amplified with barcoded universal bacterial primers targeting variable region V4 of 16SrRNA gene (515F-806R barcoded primers). The standardized protocol from the earth microbiome project was followed (Caporaso et al., 2011). DNA was amplified with QuantaBio 5Prime HotMasterMix using 515 forward primer, 806 reverse barcoded primer and 2ng template. The PCR conditions included an initial denaturation at 94°C for 3', followed by 35 cycles of denaturation at 94°C for 45'', annealing at 50°C for 1', and extension at 72°C for 90'', with a final extension at 72°C for 10'. Each PCR was performed in triplicate. The products were combined and quality checked on an agarose gel. Each PCR amplification was then quantified with Quant-iT PicoGreen dsDNA Assay with SpectraMax Gemini XPS microplate reader, and pooled to an equal amount of 200 ng per sample to form the library. The library was purified using QIAquick PCR purification Kit (Qiagen, Ref. 28104), and sequenced from both ends on Illumina MiSeq (kit v2) to generate 2x250bp paired-end reads (Illumina, San Diego, CA, USA). Demultiplexed FASTQ files were generated using the MiSeq reporter software using Qiime version 1.9.1, demultiplexed files were paired with a minimum overlap of 200 reads, and barcodes removed from the sequence. Sequences were quality filtered with phred score of 33 and chimeric sequences removed using Usearch61. OTUs were identified

using the pick_open_reference_otus command against the Greengenes 13.8 database clustered at 97%. For the downstream analysis the number of reads per sample was rarefied to the lowest count in any sample (30000).

Metagenomic Sequencing

Paired-end metagenomic libraries were prepared from 200 ng DNA using TruSeq Nano DNA Library Preparation Kit (Illumina) and size selected at about 350 bp. The pooled indexed library was sequenced in Rapid Run (RR) mode for 2x250+8 cycles on an Illumina HiSeq 2500 instrument at Fasteris (Plan-les-Ouates, Switzerland) using HiSeq Rapid SBS Kit v2 and HiSeq Control Software 2.2.58. Demultiplexed FASTQ files were generated with CASAVA-1.8.2 from on-instrument base-calling by Real-Time Analysis (RTA) software 1.18.64.0. The trimmomatic package (Bolger et al., 2014) was used to remove bases that correspond to the standard Illumina adapters. Paired reads were quality filtered and joined using PEAR v0.9.6 (Zhang et al., 2014) with the following parameters: -m 575 -n 200 -v 25 -t 120 -q 33 -p 0.0001 -u 0.

Metagenomic Functional Analysis

To filter out putative artificial replicate reads we used a home-made script which retains only the longest sequence from those with identical first 100 bases. DECONSEQ (Schmieder and Edwards, 2011) with $\geq$90% coverage and $\geq$90% identity was used to remove sequences matching mouse (Mus musculus) genome data (em_rel_std_mus). Functional assignments of sequences was made using the SEED database subsystems (levels 1–3) and functional roles (level 4) (Overbeek et al., 2005) by means of SUPER-FOCUS (Silva et al., 2016) and DIAMOND (Buchfink et al., 2015) with the following parameters: -m 1 -a diamond -mi 80 -ml 30 -db DB_100.

Microbiota Diversity

The Bray-Curtis similarity matrix, based on the square-root-transformed relative abundance of OTUs or gene functions was constructed in PRIMER (Primer-E Ltd., Plymouth, UK). Principal coordinates analysis (PCoA) of Bray-Curtis similarity matrices was performed in PRIMER. Ecological indices (diversity, richness) was calculated from the relative abundance of OTUs in PRIMER.

Microbiota Transplantation

To transplant the GF mice with microbiota, 500 μL of freshly extracted cecal contents from either *ad libitum* or caloric restricted mice were resuspended in 5 mL of anaerobic PBS and 100 μL of the solution was inoculated by oral gavage at days 0 and 2 into each mouse. Animals were kept for 7 days in dirty cages from the respective donor group. The colonization was confirmed by qPCR.

Hyperinsulinemic Euglycemic Clamp in Microbiota Transplanted Mice

We took several additional steps to avoid any disruption of the transplanted microbiota. Only single-use materials and solutions were used for each mouse, and all surgeries and catheters washing were done under ventilated hood with sterilization of the environment using Virkon S 1% solution (Arovet AG, Dietikon, Switzerland) between each mouse 1 week after the microbiota transfer. Catheters were implanted 7 days prior to the experiment in the right jugular vein and exteriorized above the neck using vascular access button (Instech Laboratories Inc, Plymouth Meeting, PA). Washing of the catheters with a sterile heparin/saline solution was performed daily. Hyperinsulinemic-euglycemic clamps were performed in conscious and unrestrained mice. Mice were fasted for 3 hr, followed by a 2-hr infusion of [3-^{3}H] glucose (0.05 μCi/min) (Perkin Elmer, Walthman, MA). Continuous insulin infusion (2.5 mIU/kg body weight/min, Actrapid, NovoNordisk A/S Bagsvaerd, Denmark) was used for the induction of hyperinsulinemia. At steady state, *in vivo* insulin-stimulated glucose uptake in tissues was determined by a 10 μCi bolus i.v. injection of 2-[^{14}C] deoxyglucose. After 30 min, mice were rapidly killed by cervical dislocation and tissues were removed and stored at −80°C until use. Glucose concentration was measured using the glucose oxidase method (GLU, Roche Diagnostics, Rotkreuz, Switzerland) and insulin using an ELISA commercial kit (CrystalChem Inc., Downers Grove, IL). Measurements of 2-[^{14}C] deoxyglucose-6-phosphate concentration in individual tissues allows calculation of the glucose utilization index in tissues. 2-[1-^{3}H]deoxyglucose (2DG) uptake measurements were performed as described in our previous publications (Chevalier et al., 2015; Suarez-Zamorano et al., 2015).

Caloric Uptake

Food intake and feces production over 24 hr was measured for each cage. Feces were subsequently collected, dried, and ground to a fine powder. Caloric excretion measurement through an oxygen bomb calorimeter and subsequent calculations were performed as previously described (Chevalier et al., 2015).

Microbiota depletion in AL and CR mice

Antibiotic treatment was performed as previously described (Suarez-Zamorano et al., 2015) and specified in Animals. Five days after the antibiotics were provided, once food intake was stabilized, caloric restriction was started following the usual protocol.

Pharmacological Treatments of Mice

LPS (either 200 or 300 μg/kg/day, Lipopolysaccharides from *Escherichia coli* 0127:B8, ref. L3129, Sigma-Aldrich) was administered for 28 days using osmotic delivery pumps (model 2004; Alzet) inserted subcutaneously into the backs of animals. CLI-095 (1 mg/kg/day, ref. tlrl-cli95, Invivogen) was injected i.p. daily for 5 weeks. The relative controls were injected daily with vehicle (10% DMSO in PBS). Intestinal alkaline phosphatase (IAP from bovine intestinal mucosa, ref. P0114, Sigma-Aldrich) was

supplemented in drinking water at a concentration of 100 units/mL). Animals were fed with HCD for 7 days before starting treatment with CLI-095 or iAP. During this initial time, no body weight changes were detected between mice allocated to the different groups.

Metabolic Experiments

Oral glucose tolerance tests were performed after 6 hr fasting by oral gavage of glucose bolus (2g/kg body weight). Insulin tolerance test was performed after a 5 hr fasting, with an intraperitoneal injection of 0.5 U/kg (for chow-fed) or 0.75 U/kg (for HCD-fed) insulin (I9278, Sigma-Aldrich). Insulin during oGTT was measured with the Mouse Insulin ELISA kit (ref. 10-1247-01, Mercodia), following the manifacturer's instruction. Body temperature measurements were performed as previously described (Fabbiano et al., 2016). All metabolic measurements were done 3 (for GF mice) or 4 weeks after starting the respective treatment.

Positron Emission Tomography-Computed Tomography (PET-CT)

Mice were anesthetized with 2% isoflurane and injected in the venous sinus with 4–5 megabecquerel (MBq) [18F]FDG. Mice were then left awake at RT during the uptake time of 20 min. 10 min prior to PET scan, mice were subjected to CT scans in a Triumph micro-PET/SPECT/CT system (TriFoil). Images were obtained at 80 peak kilovoltage (kVp) and 160 mA, and 1,024 projections were acquired during the 360 rotation with a field of view of 71.3 mm (1.73 magnification). After 20 min of [18F]FDG uptake, PET scans were started for a total duration of 10 min (Fabbiano et al., 2016). The software Osirix (Pixmeo) was used to quantitatively analyze the datasets and generate pictures.

Histological Analyses

For hematoxylin-eosin (H&E) staining, tissues were excised, fixed in 4% paraformaldehyde (Sigma-Aldrich), paraffin embedded, cut in 5 μm-thick sections and stained with H&E using standard techniques. Immunohistochemical detection of UCP1 was performed on paraffin section using a standard protocol with the following changes: citrate buffer antigen retrieval in defrost-mode microwave for 15'; blocking for 60 min at RT with 2% BSA; overnight incubation at 4°C with primary rabbit anti-UCP1 antibody (Pierce PA1-24894, 1:100) and 45′secondary antibody incubation (Goat anti-Rat IgG (H+L) Secondary Antibody, Alexa Fluor 488 conjugate, Thermo Fisher Scientific A-11006, 1:500) For mucin layer thickness measurement, freshly excised colons were fixed in Carnoy for 4 hr at room temperature and then stored in ethanol until processing. After embedding and cutting in 5 μm-thick sections, samples were stained with Alcian Blue and counterstained with Nuclear Fast Red-Aluminum. The mucin layer was quantified blindly by taking hundreds of measurements, using the Metamorph software, throughout the whole colon length in regions containing fecal masses (Desai et al., 2016).

RNA Extraction, Retrotranscription and Real-Time PCR

Frozen tissues were placed in 2 mL eppendorf tubes containing 1 mL Trizol (Thermo Fisher Scientific) and mechanically disgregated using the bead-based TissueLyser equipment (Qiagen) by shaking for 30 s at 30 Hz in presence of one bead per tube. After brief centrifugation to remove tissue debris (3 min at 2000 RPM at 4°C), 300 μL chloroform were added, samples were shaken and centrifuged for 10 min at 10000 RPM at 4°C. The chloroform phase was collected, mixed with 600 μL isopropanol and centrifuged again as before. The pellet obtained was washed twice with 70% ethanol and finally resuspended in 50 μL PCR-grade water. For retrotranscription, 1 μg RNA was used per sample using the High-Capacity cDNA Reverse Transcription Kit (Applied Biosystems). qPCR were performed on a LightCycler 480 machine (Roche) with SYBR Green-based detection (Roche). The primer sequences are shown in the Key Resources Table.

Oxygen Consumption Rate (OCR)

Inguinal adipose pads were excised and washed in fresh-made ice-cold respiration buffer (2.5 mM glucose, 4 mM KCl, 115 mM NaCl, 20 mM Tris HCl, 1 mM MgCl2, 1.5 mM KH2PO4, 2 mM MgSO4, 1.5 mM $CaCl_2$, at pH 7.4) supplemented with 2% fatty acid-free BSA. After removing non-adipose material and excess of lipids, tissues were cut into 2.5-5 mg pieces using a 2.5 mm biopsy punch avoiding visible vasculature. After two additional washes without fatty acid-free BSA, tissue biopsies were placed in Islet Capture Plates and covered with the screen and 450 μL of respiration buffer supplemented with 25 mM HEPES. The plate was allowed to equilibrate for 45 min at 37°C without CO_2 before reading in a Seahorse Analyzer (model XFe24, Seahorse Bioscience) (Fabbiano et al., 2016). The software was programmed for 4 cycles of 3 min mix; 2 min rest; 3 min measurements in basal and stimulated conditions (10 μM Isoproterenol, Sigma-Aldrich).

Flow Cytometry and Characterization of Hematopoietic Cell Populations

Primary stromal vascular fractions (SVF) from adipose tissues were prepared as following: mice were sacrificed and the inguinal fat pads quickly excised and placed in cold PBS. After removal of the lymph nodes, fat tissues were digested for 30 min in collagenase I (4 mg/mL in DMEM) at 37°C. Samples were subsequently centrifuged, the pellet was resuspended in DMEM and filtered through a 0.45 μm mesh and centrifuged again. Single cells preparations were washed in phosphate-buffered saline (PBS) supplemented with 0.1% BSA and 0.5 mM EDTA, pH 8.0, and stained either with rat monoclonal anti-F4/80 (Clone A3-1, cat # ab105155, 1:200, Abcam), rat monoclonal anti-CD11b (Clone M1/70, cat # 561114, 1:200, BD Biosciences), and rat monoclonal anti-CD301 (MGL1/MGL2) (Clone LOM-14, cat # 145705, 1:400, BioLegend) for macrophage stainings; rat monoclonal anti-CD45 (Clone 104, cat #558702, 1:200, BD Biosciences) or rat monoclonal anti-CD11b (Clone M1/70, cat # 561114, 1:200, BD Biosciences) and rat monoclonal

anti-Siglec F (Clone E50-2440, cat # 562068, 1:200, BD Biosciences) for eosinophil staining. All centrifuge steps were performed at 4°C for 5 min at 1700 RPM. Data were acquired using a Gallios Flow Cytometer (Beckman Coulter) and analyzed with FlowJo v10 software. After gating out dead cells and doublets, macrophages were identified as $CD11b^+F4/80^+$ and eosinophils as $CD45^+$ Siglec-F^+ cells (Sun and Trajkovski, 2014; Trajkovski et al., 2012; Fabbiano et al., 2016).

Endotoxin Measurement

Serum endotoxin was determined with either the LAL Chromogenic Endotoxin Quantitation kit (Pierce) or with an Endosafe-PTS machine (Charles River Microbial solutions) using 0.005 EU/mL cartridges. In all cases, sera were diluted 1:10-1:100 in pyrogen-free conditions and inactivated for 10 min at 70°C. Spiking and recovery rates were used to confirm the absence of inhibition in the tested samples. Fecal samples were measured with the Chromogenic Kit as above with a modified protocol from (Kim et al., 2012): fecal pellets were placed in 10 mL in a pyrogen-free tube and sonicated for 60 min , then centrifugated at 400 g for 15 min , filtrated through a 0.22 μm filter, diluted 1:1000 in pyrogen-free water and inactivated for 10 min at 70°C. Samples were then assayed following the standard kit protocol.

Bone Marrow Transplantations (BMT)

8-week-old recipient WT CD45.1 and $Tlr4^{-/-}$ mice (which possess the CD45.2 variant) were lethally irradiated with 1000 rads. 24 hr after, animals were reconstituted via tail vein injection with 5×10^6 bone marrow hematopoietic cells collected from donor mice. Mice were treated with Baytril 10% (6 mL/L drinking water) for the following two weeks to prevent infections. Five weeks after tail vein injection, the reconstitution was confirmed by analyzing the presence of CD45.1 or CD45.2 in peripheral blood of recipient mice. Animals were kept under HCD and all *in vivo* experiments were carried out 7-8 weeks after bone marrow transplant.

Hyperinsulinemic Euglycemic Clamp

Euglycemic-hyperinsulinemic clamps were performed in conscious, unrestrained, catheterized mice at the glucose- insulin clamp platform, University of Geneva. Seven days before the experiment, mice were anesthetized using isoflurane, and a silastic catheter (0.012 inch inner diameter) was surgically implanted in the right jugular vein and exteriorized above the neck using vascular access button (Instech Laboratories Inc., Plymouth Meeting, PA). Mice were fasted for 5 hr before the start of the experiment (t = 0 min). At $t = -120$ min, an infusion of [1-3H] glucose (0.05 Ci per min) (PerkinElmer, Waltham, MA, USA) was initiated. After 120 min, blood samples were collected from the tail vein to measure basal blood glucose and plasma insulin as well as to calculate the rate of endogenous glucose appearance (EndoRa) and glucose disposal (Rd) at basal state. At t = 0 min, a continuous insulin infusion (2.5 mIU per kg body weight per min) (NovoRapid, Novo Nordisk Pharma, Zurich, Switzerland) was used to induce hyperinsulinemia. The infusion of [3-3H] glucose was increased to 0.1 Ci per min and 50% glucose was infused to maintain target euglycemia (120 mg per dL) (glucose infusion rate, GIR). At steady state, insulin- stimulated glucose uptake in tissues *in vivo* was determined by using a 10 Ci bolus injection of 2-[14C]deoxyglucose (2-[14C]DG) (PerkinElmer). After 30 min, mice were killed by cervical dislocation and tissues were removed and stored at −80°C until use. [3-3H]glucose and 2-[14C]DG specific activities were determined in deproteinized blood samples. Plasma insulin was measured by ELISA (Mercodia, Uppsala, Sweden). EndoRa under an insulin-stimulated state was determined by subtracting steady-state GIR from Rd. Measurements of 2-[14C]deoxyglucose-6-phosphate concentration enabled calculation of the glucose utilization index of individual tissues.

Intestinal Permeability Assay

Dextran-FITC (4 kDa, 10 μL/g BW, Ref. 46944-500MG-F, Sigma-Aldrich) was gavaged to mice in the morning. Animals were subsequently fasted and 4 hr later 30 μL of blood were collected from the tail. After centrifugation to obtain serum, 15 μL of each sample was diluted to 100 μL with water and samples were placed in a black bottom 96-well plate. A standard curve was obtained by serial dilutions of the stock dextran-FITC and concentrations were calculated by detecting fluorescence at 525 μm.

Liver Triglycerides Detection

For each mouse, 50 mg of liver tissue were incubated in methanol/chloroform mix (25 μL and 200 μL, respectively) for 4 hr at 40°C shaking. The chloroform phase was subsequently evaporated by centrifuging samples in a SpeedVac vacuum concentrator (Eppendorf) at room temperature for 1 hr. Samples were then resuspended in 70% ethanol and incubated at 50°C for 30 min. Triglyceride determination was then performed using the Serum Triglyceride Determination Kit (Cat. TR-0100, Sigma Aldrich) using water as blank control and a glycerol standard solution for the standard curve (Cat. G7793, Sigma Aldrich) following the manufacturer instructions.

QUANTIFICATIONS AND STATISTICAL ANALYSIS

Unless otherwise specified in the figure legends, significance was calculated using non-paired two tailed Student's t test. For all figures, $^*p \leq 0.05$, $^{**}p \leq 0.01$, $^{***}p \leq 0.001$. Error bars show standard deviation, unless otherwise stated. Sample sizes and animal numbers were chosen based on power calculations of 0.8. All experiments, except for 16S and metagenomic study, were independently performed at least three times without blinding, and representative values from one experiment are shown. No animals or values were excluded from the analysis. To assess differences in microbiota composition between pre-defined groups of samples, we used permutational multivariate analysis of variance (PERMANOVA, PRIMER) of the Bray-Curtis similarity matrix. In addition,

Wilcoxon rank-sum and Wilcoxon signed-rank tests were used to assess statistical significance of differences in the proportion of individual taxa or gene functions between pre-defined groups of samples. Statistical significance was set at the 95% confidence level ($p < 0.05$) and no correction was applied for multiple testing.

Graphical Design

The graphical abstract was designed using images available from Servier Medical Art, licensed under a Creative Common Attribution 3.0 Generic License http://smart.servier.com/.

DATA AND SOFTWARE AVAILABILITY

The accession number for the metagenomics and 16S rDNA sequencing data reported in this paper is NCBI, short read archive (SRA): PRJNA480387.